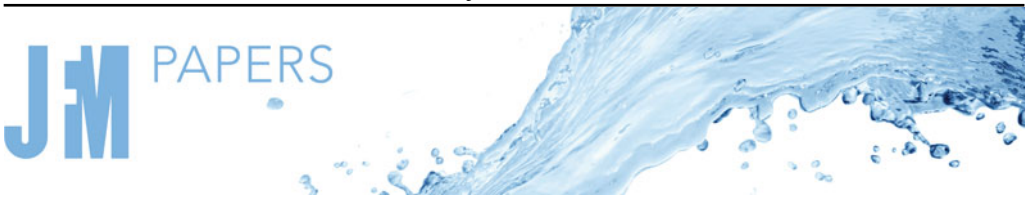
J. Fluid Mech. (2026), *vol.* 1043, A10, doi:10.1017/jfm.2026.12013



Secondary global instabilities in shock-wave–boundary-layer interactions: direct numerical simulations and three-dimensional global stability analysis

Ziming Song[1], **Jiaao Hao**[1], **Ismaïl Ben Hassan Saïdi**[2] and **Jean-Christophe Robinet**[2]

[1]Department of Aeronautical and Aviation Engineering, The Hong Kong Polytechnic University, Kowloon, Hong Kong SAR

[2]Laboratoire DynFluid, Arts et Métiers ParisTech, 151 boulevard de l'Hôpital, 75013 Paris, France

Corresponding author: Jiaao Hao, jiaao.hao@polyu.edu.hk

(Received 22 March 2026 UTC; revised 29 July 2026 UTC; accepted 6 August 2026 UTC)

Secondary instabilities developing from the stationary primary global mode are investigated for an incident shock flow at Mach 2.15. Direct numerical simulations (DNS) and three-dimensional global stability analysis (3-D GSA) are combined to elucidate the evolution and characteristics of the associated secondary branches. Two spanwise domain widths are considered, λ_m and $2\lambda_m$, where λ_m denotes the spanwise wavelength of the primary global mode. In the λ_m domain, a time-periodic unsteadiness emerges as a secondary instability after saturation of the primary global mode, which is identified as a supercritical Hopf bifurcation. In the $2\lambda_m$ domain, an additional secondary growth accompanied by wavelength doubling is observed following the onset of unsteadiness. A corresponding stationary secondary instability with wavelength $2\lambda_m$ is determined to be the mechanism underlying this secondary growth, which is a subcritical pitchfork bifurcation. Overall, DNS and 3-D GSA provide a consistent interpretation of the secondary-instability scenario, and highlight the sensitivity of the observed dynamics to the spanwise domain width.

Key words: high-speed flow, absolute/convective instability, boundary layer stability

© The Author(s), 2026. Published by Cambridge University Press. This is an Open Access article, distributed under the terms of the Creative Commons Attribution licence (https://creativecommons.org/licenses/by/4.0/), which permits unrestricted re-use, distribution and reproduction, provided the original article is properly cited.

https://doi.org/10.1017/jfm.2026.12013 Published online by Cambridge University Press

1. Introduction

Shock-wave–boundary-layer interactions (SWBLIs) represent a fundamental and challenging phenomenon in high-speed aerodynamics, commonly encountered in transonic wings, supersonic inlets and turbomachinery blades (Sabnis & Babinsky 2023). In these practical configurations, SWBLIs induce complex flow features, including boundary-layer separation, unsteady shock motion and severe pressure and thermal loads. These effects further complicate the physical understanding of SWBLIs, and constitute a persistent bottleneck in aircraft design.

Systematic research on SWBLIs can be traced back to the 1940s, driven by the emergence of transonic flight and the development of capable wind tunnel facilities. Early foundational work combined experimental visualisation with theoretical modelling. Donaldson (1944), Liepmann (1946) and Ackeret *et al.* (1947) were among the first to experimentally document the key flow structures of SWBLIs. Building upon earlier ideas of Lighthill (1953), Gadd (1957) and Chapman *et al.* (1958), Stewartson & Williams (1969) established the comprehensive asymptotic theory of free interaction, which was confirmed by the detailed experimental measurements of Erdos & Pallone (1962). Subsequent contributions (Reyhner & Flügge-Lotz 1968; Hankey & Holden 1975; Délery *et al.* 1986; Degrez *et al.* 1987; Stanewsky 1988) further shaped the general understanding of SWBLIs.

However, the aforementioned studies predominantly focused on the static or time-averaged characteristics of SWBLIs and therefore cannot fully explain certain dynamic phenomena in high-speed flights, such as transonic wing buffet and inlet buzz. Although SWBLI unsteadiness was reported as early as the 1950s (Chapman *et al.* 1958), progress on this topic was long hindered by the limited experimental measurement techniques (Dolling 2001). It was not until the early 1990s that the inherent unsteadiness in SWBLIs began to receive substantial attention. In the context of turbulent interactions, experiments across a variety of configurations consistently captured low-frequency motions, manifesting as shock-foot oscillation and periodic ‘breathing’ of the separation bubble (Erengil & Dolling 1991; Brusniak & Dolling 1994; Dupont *et al.* 2006; Dussauge *et al.* 2006). A defining signature of this unsteadiness is its dominant low-frequency content, typically one to two orders of magnitude lower than the characteristic turbulence frequencies in the incoming boundary layer. The origins of the unsteadiness are generally categorised into two types: upstream and downstream mechanisms. The upstream mechanism is associated with the interaction of large-scale structures in the upstream boundary layer (Ganapathisubramani *et al.* 2007), while the downstream mechanism attributes the unsteadiness to the intrinsic dynamics of the recirculation bubble (Dussauge & Piponniau 2008).

More recent research indicates that both the upstream and downstream mechanisms contribute to this unsteadiness, with their relative importance depending on the interaction strength and separation length. Clemens & Narayanaswamy (2014) noted that the two mechanisms appear to be closely linked to the scale of separation, with larger separation bubbles tending to strengthen the influence of the downstream mechanism. Nichols *et al.* (2017) employed both linear (global stability analysis, GSA) and nonlinear (dynamic mode decomposition) analyses of turbulent SWBLIs, and attributed the low-frequency motion to a damped, oscillatory intrinsic mode excited by upstream disturbances. Hao (2023) combined GSA and resolvent analysis, showing that the low-frequency unsteadiness arises from modal resonance between the leading global mode and external forcing. In transitional SWBLIs, Ben Hassan Saïdi *et al.* (2025) proposed a triadic mechanism to explain the unsteadiness and the bubble ‘breathing’, which involves nonlinear saturation of the convective instabilities in the shear layer, and the upstream propagation of

https://doi.org/10.1017/jfm.2026.12013 Published online by Cambridge University Press

perturbations within the separation bubble. Mauriello *et al.* (2025) imposed two oblique modes with closely spaced frequencies such that their difference fell within the low-frequency band of unsteadiness, and showed that the low-frequency unsteadiness can be generated by quadratic nonlinear interactions that produce a difference-frequency component between the two oblique waves.

In contrast to turbulent and transitional interactions, unsteadiness in laminar SWBLIs received much less attention, despite the practical significance and diverse underlying mechanisms. Laminar interactions can trigger boundary-layer transition (Kachanov 1994) and thereby induce substantial changes in aerodynamic performance, including increased skin-friction drag and aero-heating loads. With the advancement of high-fidelity numerical simulations and linear stability theory (LST) (Malik 1989; Zhong & Wang 2012) for high-Mach-number boundary layers, the instability mechanisms of laminar SWBLIs have been increasingly examined.

Early studies of instability in laminar boundary layers mainly focused on convective instabilities. Within this framework, external disturbances penetrate the boundary layer through receptivity processes (Fedorov & Khokhlov 1991) and are subsequently amplified as they convect downstream. Representative examples are the classical instability families of high-speed boundary layers, namely Mack's first and second modes (Mack 1984). Fundamental studies on the stability of high-speed shear layers and boundary layers (Sandham & Reynolds 1991; Balakumar & Malik 1992; Fasel *et al.* 1993; Chang & Malik 1994) clarified the mechanisms of convective instabilities and three-dimensional (3-D) breakdown to turbulence on flat plates. These mechanisms remain highly relevant to SWBLI dynamics. Pagella *et al.* (2004) conducted a comparative investigation of the instability characteristics between compression corner and incident shock flows using LST and two-dimensional (2-D) direct numerical simulations (DNS). Balakumar *et al.* (2005) employed LST and DNS to track the evolution of the second mode along a compression corner with separation. Sandham *et al.* (2014) combined experiments and DNS to examine transition triggered by the interaction of the second mode and streaks in an incident shock flow at Mach 6, while Lugrin *et al.* (2021) carried out DNS of transition over an axisymmetric compression ramp at Mach 5, attributing the breakdown to nonlinear interactions among oblique modes.

Regarding the role played by SWBLIs in transition, it is now recognised as an efficient amplifier for both convective- and component-type instabilities. To systematically analyse such amplification behaviour, resolvent analysis is a powerful tool to identify the optimally amplified disturbances, as it accounts for the non-normality of the linear operator, and does not require the parallel-flow assumption. Using this approach, Dwivedi *et al.* (2019) attributed the amplification of streaks over a compression ramp to streamwise deceleration and baroclinic effects. Subsequent work demonstrated that the amplification of oblique waves is driven by flow curvature and contributes to transition processes through nonlinear interactions (Dwivedi *et al.* 2022). Further resolvent studies include the identification of the most amplified modes in a compression corner flow at Mach 7.7 (Hao *et al.* 2023), and an investigation of the amplification mechanisms of streaks, the first mode and the second mode in equivalent compression corner and incident shock flows at Mach 6 (Song & Hao 2025). Savarino *et al.* (2024) employed nonlinear resolvent analysis to demonstrate the nonlinear interaction between a pair of oblique modes and its role in promoting transition in an incident shock flow at Mach 2.15.

In addition to acting as an amplifier, SWBLIs can also behave as a self-sustained oscillator, governed by intrinsic (global) instabilities. Such behaviour emerges when the interaction strength exceeds a critical threshold, typically measured by the shock intensity or the size of the separation bubble (Hildebrand *et al.* 2018; Sidharth *et al.* 2018; Hao *et al.*

https://doi.org/10.1017/jfm.2026.12013 Published online by Cambridge University Press

2021; Li & Hao 2023). To explore this mechanism, Robinet (2007) applied 2-D GSA to an incident shock flow at Mach 2.15. In the global framework, no external disturbance is introduced, and the base flow is assumed to be inhomogeneous in two directions, and homogeneous in the third. Under a modal assumption of the perturbation, the linearised Navier–Stokes (LNS) equations can be cast as an eigenvalue problem for global modes. Robinet's work identified a stationary global mode in SWBLIs, whose destabilisation marks a primary bifurcation that drives the flow from a 2-D state to a 3-D configuration. Additional DNS reported unsteadiness after the saturation of this global mode at certain shock angles and for specific spanwise domain widths, indicating the onset of a secondary bifurcation.

The classification of such bifurcations is a crucial concept for nonlinear dynamical systems because it specifies the nature of a new state that emerges. A steady bifurcation (e.g. a pitchfork bifurcation) leads to a new steady solution, often breaking a spatial symmetry. By contrast, a Hopf bifurcation gives rise to time-periodic oscillations. A further critical distinction lies in how these bifurcations occur: a supercritical bifurcation produces a new branch that evolves smoothly from the original state, whereas a subcritical bifurcation is associated with an abrupt transition, hysteresis, and potentially drastic changes in the flow state. This classification framework is essential for interpreting more complex dynamics, as demonstrated more recently by Song & Hao (2023), who refined the stability analysis and DNS of Robinet (2007) with higher resolution. A more intricate scenario is revealed: after the saturation of the primary global mode, the flow not only becomes unsteady but also exhibits a secondary growth of perturbation. This secondary growth is accompanied by wavelength doubling, such that the dominant spanwise wavelength becomes twice that of the primary unstable mode. The wavelength doubling is further confirmed in a wider domain with width four times the spanwise wavelength of the primary global mode. These observations raise a natural question: what is the origin of this unsteadiness and secondary growth? To address this question, the present study applies 3-D GSA to the 3-D base flow that develops after the primary global mode saturates.

To the best of the authors' knowledge, this study presents the first application of 3-D GSA analysis to supersonic SWBLIs. The 3-D GSA extends the 2-D global framework by allowing spatial inhomogeneity of the base flow in all three directions, thereby enabling the capture of 3-D flow dynamics. Since its introduction, the approach has proven powerful in uncovering complex bifurcation phenomena and intrinsic instabilities across a wide range of flow configurations, including sphere wakes (Tezuka & Suzuki 2006), cavity flows (Giannetti *et al.* 2009), jet–crossflow interactions (Bagheri *et al.* 2009) and roughness-induced transitions (Loiseau *et al.* 2014). Notably, Sansica *et al.* (2018) identified a secondary Hopf bifurcation in an incompressible sphere flow at Mach 0.1 using 3-D GSA. Extending this work, Sansica *et al.* (2020) reported a supersonic counterpart of the Hopf bifurcation in compressible sphere wakes at higher Mach number 1.2. Rodríguez *et al.* (2021) identified a secondary oscillatory instability in incompressible laminar separation bubbles on a flat plate using DNS and cross-plane stability analysis, which is an extension of the classic weakly non-parallel stability analysis. He & Timme (2021) applied 3-D GSA to a turbulent transonic infinite-wing configuration, using Reynolds-averaged Navier–Stokes base flows, to uncover the mechanisms underlying shock buffet. Frantz *et al.* (2025) demonstrated the presence of a secondary Hopf bifurcation ('Neimark–Sacker bifurcation') in addition to the pitchfork and Hopf bifurcations in cube and sphere wakes.

The aforementioned research on instability in 3-D flows has, however, primarily focused on low-Mach-number and wake-type flows, with little attention paid to supersonic SWBLIs. Motivated by this research gap and the complex behaviour observed in Robinet

https://doi.org/10.1017/jfm.2026.12013 Published online by Cambridge University Press

(2007) and Song & Hao (2023), the present work aims to (i) reveal the mechanisms responsible for the unsteadiness and the secondary growth, (ii) determine the associated bifurcation types, and (iii) characterise the secondary instabilities in separation bubbles induced by SWBLIs. The remainder of this paper is organised as follows. Section 2 describes the numerical methods, including DNS and GSA. Section 3 provides the computational set-up. Section 4 presents results across different spanwise domain widths. Section 5 discusses and summarises the main conclusions.

2. Numerical methods

2.1. *The DNS*

The governing equations for DNS are the 3-D compressible Navier–Stokes equations, which can be expressed in the form

$$\frac{\partial \boldsymbol{U}}{\partial t} + \frac{\partial \boldsymbol{F}_j}{\partial x_j} = \frac{\partial \boldsymbol{F}_{v,j}}{\partial x_j}, \tag{2.1}$$

where

$$\boldsymbol{U} = \begin{pmatrix} \rho \\ \rho u_i \\ \rho e \end{pmatrix}, \quad \boldsymbol{F}_j = \begin{pmatrix} \rho u_j \\ \rho u_i u_j + p\delta_{ij} \\ (\rho e + p)u_j \end{pmatrix}, \quad \boldsymbol{F}_{v,j} = \begin{pmatrix} 0 \\ \tau_{ij} \\ \tau_{ij} u_i + q_j \end{pmatrix} \tag{2.2}$$

are the vectors of conservative variables, inviscid fluxes and viscous fluxes, respectively. Further details of the governing equations can be found in Song & Hao (2023).

The Navier–Stokes equations are solved using an in-house finite-volume solver PHAROS (Hao *et al.* 2016; Hao & Wen 2020). The inviscid fluxes are discretised with the Harten–Lax–van Leer contact scheme (Harten *et al.* 1983; Toro *et al.* 1994), employing seventh-order linear upwind reconstruction in smooth regions, and second-order MUSCL reconstruction (van Leer 1979) in regions with discontinuities. The switching between these reconstruction strategies is controlled by the modified Ducros shock sensor (Hendrickson *et al.* 2018). Viscous fluxes are calculated using a second-order central scheme. Time integration is performed with a third-order Runge–Kutta method using time step 20 ns, corresponding to CFL number 0.7. Recently, PHAROS has been ported to CUDA Fortran, enabling GPU acceleration and substantially improving computational efficiency.

2.2. *The GSA*

Within linear stability analysis, the vector of conservative variables $\boldsymbol{U}$ is decomposed into a steady base-flow solution $\overline{\boldsymbol{U}}$ and an infinitesimal perturbation $\boldsymbol{U}'$ as

$$\boldsymbol{U}(x, y, z, t) = \overline{\boldsymbol{U}}(x, y, z) + \boldsymbol{U}'(x, y, z, t). \tag{2.3}$$

The LNS equations are obtained by substituting (2.3) into (2.1) and neglecting high-order terms:

$$\frac{\partial \boldsymbol{U}'}{\partial t} + \frac{\partial \boldsymbol{F}'_j}{\partial x_j} = \frac{\partial \boldsymbol{F}'_{v,j}}{\partial x_j}. \tag{2.4}$$

https://doi.org/10.1017/jfm.2026.12013 Published online by Cambridge University Press

After spatial discretisation and separation of spatio-temporal dependencies, the LNS equations can be expressed as a system of ordinary differential equations as

$$\frac{\mathrm{d}\boldsymbol{U}'}{\mathrm{d}t} = \boldsymbol{A}\boldsymbol{U}'. \tag{2.5}$$

Here, $\boldsymbol{A}$ denotes the Jacobian matrix determined by the steady base flow.

2.2.1. *The 2-D GSA*

In 2-D GSA, the perturbation $\boldsymbol{U}'$ is assumed to be periodic in the spanwise direction, thus it can be expressed in the modal form

$$\boldsymbol{U}'(x,\, y,\, z,\, t) = \mathrm{Re}\left\{\hat{\boldsymbol{U}}(x,\, y)\, \mathrm{e}^{\mathrm{i}\beta z - \mathrm{i}\omega t}\right\}. \tag{2.6}$$

Here, $\mathrm{Re}\{\cdot\}$ denotes the real part of a complex-valued quantity, $\hat{\boldsymbol{U}}$ is the 2-D eigenmode, β is the spanwise wavenumber, and $\omega = \omega_r + \mathrm{i}\omega_i$ is the corresponding eigenvalue. Substituting (2.6) into (2.5) results in an eigenvalue problem:

$$\boldsymbol{A}(\beta)\, \hat{\boldsymbol{U}} = -\mathrm{i}\omega \hat{\boldsymbol{U}}. \tag{2.7}$$

The Jacobian matrix $\boldsymbol{A}$ is constructed using a second-order spatial discretisation. Specifically, the inviscid Jacobians are computed with the modified Steger–Warming flux splitting scheme (MacCormack 2014) in the vicinity of discontinuities, while a central scheme is applied in smooth regions. The eigenvalues of matrix $\boldsymbol{A}$ for a given wavenumber β are obtained using the Arnoldi method implemented in ARPACK (Sorensen *et al.* 1996). The linear systems arising in the shift-invert Arnoldi iterations are solved by performing LU factorisation with the MUMPS package (Amestoy *et al.* 2001, 2019).

2.2.2. *The 3-D GSA*

In 3-D GSA, the Jacobian matrix $\boldsymbol{A}$ is prohibitively large to be decomposed explicitly. Instead, it is worth noting that (2.5) admits the formal solution

$$\boldsymbol{U}'(t) = \mathrm{e}^{\boldsymbol{A}t}\, \boldsymbol{U}'(0) = \sum_k c_k \hat{\boldsymbol{U}}_k\, \mathrm{e}^{-\mathrm{i}\omega_k t}, \tag{2.8}$$

where $\omega_k = \omega_{r,k} + \mathrm{i}\omega_{i,k}$ is an eigenvalue of $\boldsymbol{A}$, and $\hat{\boldsymbol{U}}_k$ is the corresponding eigenmode. The stability problem thus again turns into an eigenvalue problem of the matrix $\boldsymbol{A}$. Instead of explicitly constructing and factorising $\boldsymbol{A}$ as in the shift-invert method, we therefore adopt a time-stepping (matrix-free) approach, in which the action of $\boldsymbol{A}$ is assessed implicitly by time integration of the linearised system (Barkley *et al.* 2008; Theofilis 2011). Defining the propagator $\boldsymbol{G}_{\Delta\tau}$ over one time interval $\Delta\tau$ as

$$\boldsymbol{G}_{\Delta\tau} = \mathrm{e}^{\boldsymbol{A}\,\Delta\tau}, \tag{2.9}$$

the perturbation evolves as

$$\boldsymbol{U}'(t + \Delta\tau) = \boldsymbol{G}_{\Delta\tau}\, \boldsymbol{U}'(t). \tag{2.10}$$

Successive applications of $\boldsymbol{G}_{\Delta\tau}$ to an arbitrary initial perturbation $\boldsymbol{U}_0$ build a Krylov subspace

$$\mathcal{K}_m = \mathrm{span}\left\{\boldsymbol{U}_0,\, \boldsymbol{G}_{\Delta\tau}\boldsymbol{U}_0,\, \boldsymbol{G}_{\Delta\tau}^2\boldsymbol{U}_0,\, \ldots,\, \boldsymbol{G}_{\Delta\tau}^{m-1}\boldsymbol{U}_0\right\}. \tag{2.11}$$

The Arnoldi algorithm implemented in ARPACK (Sorensen *et al.* 1996) is then applied to the Krylov subspace. This procedure yields Ritz pairs $(\mu_k,\, \boldsymbol{y}_k)$, which provide

https://doi.org/10.1017/jfm.2026.12013 Published online by Cambridge University Press

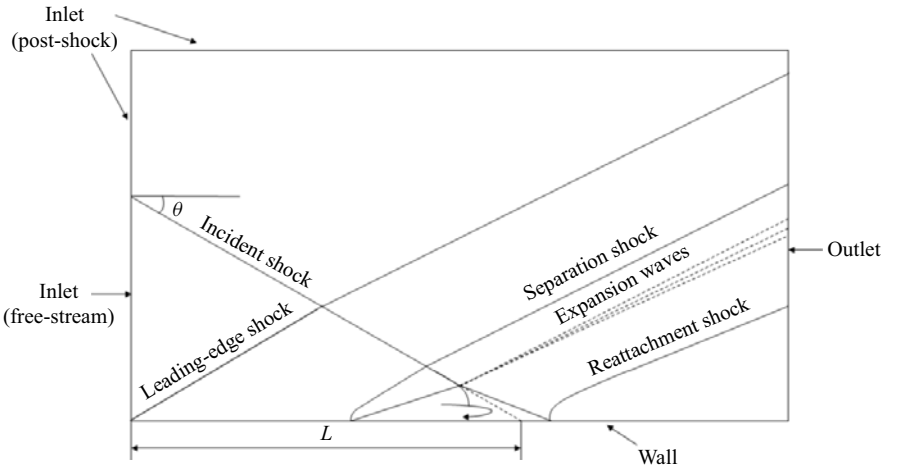


Figure 1. Schematic of an incident shock flow and the applied boundary conditions.

approximations to the eigenpairs of $\boldsymbol{G}_{\Delta\tau}$. The corresponding eigenvalues and eigenmodes of $\boldsymbol{A}$ are recovered via

$$\omega_k = \frac{\mathrm{i}}{\Delta\tau}\ln(\mu_k), \quad \hat{\boldsymbol{U}}_k \approx \boldsymbol{V}_m \boldsymbol{y}_k, \tag{2.12}$$

where $\boldsymbol{V}_m$ is the orthogonal basis matrix of the Krylov subspace.

The Jacobians in 3-D GSA are discretised using the same strategy as in the 2-D GSA described above. The time propagator $\boldsymbol{G}_{\Delta\tau}$ is constructed with a second-order Runge–Kutta method with constant sub-time interval 20 ns, corresponding to CFL number 0.7. In each Arnoldi iteration, the linearised system is integrated for one characteristic flow time (160 µs) within 8000 substeps. The Krylov subspace dimension is set to $m = 50$. The 3-D GSA also makes use of GPU acceleration.

3. Computational set-up

The configuration considered in this study is an incident shock flow, as shown in figure 1. The flow conditions are identical to those used in Robinet (2007) and Song & Hao (2023), originally based on the experiment of Degrez *et al.* (1987). The free-stream parameters are $M_\infty = 2.15$, $p_\infty = 1028$ Pa, $T_\infty = 153.33$ K, $Re_\infty = 1.25 \times 10^6$ m^{-1}. The inviscid incident position is $L = 80$ mm, corresponding to Reynolds number 1×10^5. In the following, the length L is used as the characteristic length scale to maintain consistency with Degrez *et al.* (1987), Robinet (2007) and Song & Hao (2023).

The shock incidence is imposed through segmented boundary conditions. At the left-hand boundary below the incident point, the inlet parameters are specified as the free-stream values described before. Above the incident point, including the upper boundary, the post-shock flow state obtained from the oblique shock relations is applied. At the right-hand boundary, an outlet condition based on simple extrapolation is imposed. On the wall, no-slip and adiabatic conditions are enforced. In the spanwise direction, periodic boundary conditions are applied in the 3-D DNS and GSA. For all grids used in this study, the height of the first cell in the wall-normal direction is set to 1.5×10^{-5} m. Details of the grid resolutions are provided in the relevant sections.

https://doi.org/10.1017/jfm.2026.12013 Published online by Cambridge University Press

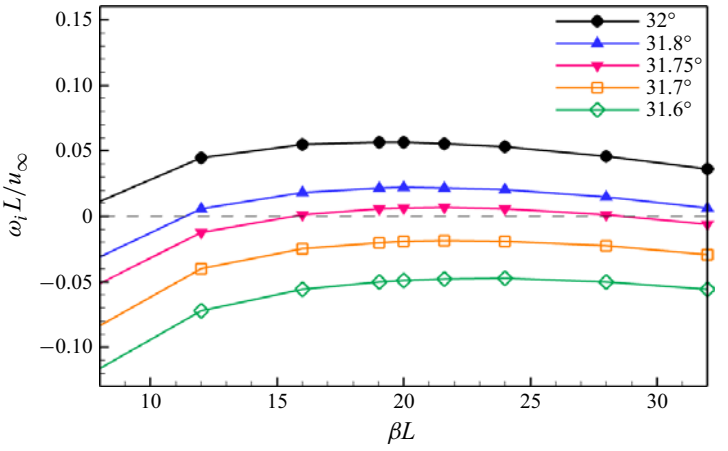


Figure 2. Variations of growth rates with spanwise wavenumbers of the most unstable modes at different incident angles.

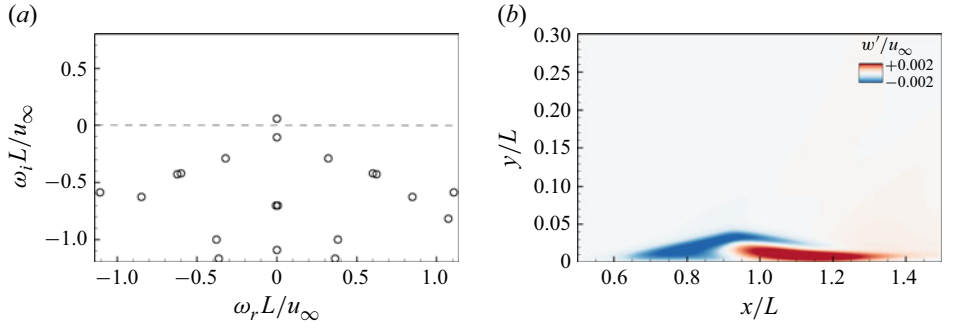


Figure 3. (*a*) Eigenvalue spectrum of $\beta_m L = 19$ at $\theta = 32°$ obtained from 2-D GSA. (*b*) Real part of spanwise velocity perturbation w' for the most unstable mode.

4. Results

4.1. *Revisiting the primary bifurcation*

In the incident shock flow as shown in figure 1, the induced separation bubble can sustain an intrinsic global mode once the shock angle θ exceeds a certain value. For moderately large shock angles, this global mode gives rise to a stationary instability. As the angle increases further, oscillatory modes emerge. In Song & Hao (2023), the critical shock angle for this globally unstable mode was determined, and its characteristics were examined in detail using a grid of 600×300 cells in the streamwise and wall-normal directions. Specifically, the critical angle was found to lie between 31.7° and 31.8°.

In the present study, the grid of 600×200 cells in the streamwise and wall-normal directions is verified to obtain grid-independent results as reported in § A.1. The growth rates of the most unstable modes as a function of spanwise wavenumber at different angles are shown in figure 2. The critical angle is estimated to be $\theta_c \approx 31.74°$ through linear interpolation between 31.7° and 31.75°. A small increase of shock angle yields a slightly globally unstable flow (e.g. $\theta = 31.75°$). At $\theta = 32°$, the maximum growth rate occurs at $\beta_m L = 19$, and the corresponding eigenvalue spectrum is shown in figure 3(*a*). The leading

https://doi.org/10.1017/jfm.2026.12013 Published online by Cambridge University Press

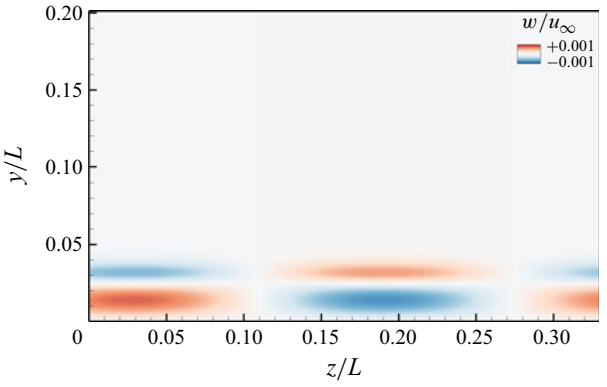


Figure 4. Spanwise velocity contour of initial flow of the $x/L = 1$ slice obtained by superimposing the 2-D GSA eigenmode onto the 2-D base flow at $\theta = 32°$.

unstable mode has zero frequency, indicating that this instability remains stationary. The associated eigenmode is presented in figure 3(*b*).

In Song & Hao (2023), DNS were performed at $\theta = 32°$ with a spanwise domain width equal to twice the wavelength $\lambda_m = 2\pi/\beta_m$ of the most unstable mode. After the saturation of the primary global mode, a secondary growth was observed in the saturated 3-D bifurcated flow, accompanied by a doubling of the spanwise wavelength. Moreover, unsteadiness appeared at a later stage of the simulation, despite the presence of only a single stationary global mode (see Song & Hao (2023) for a more detailed description). These observations raise an intriguing question: what is the origin of this secondary growth and the subsequent unsteadiness? Addressing this question is the primary objective of the present study. To this end, we first consider a simpler configuration in which the spanwise domain width is restricted to λ_m, so that the secondary growth is suppressed. We then extend the analysis to spanwise width $2\lambda_m$, which allows both secondary growth and unsteadiness for further investigation. As reported by Song & Hao (2023), the dynamics observed in the $2\lambda_m$ and $4\lambda_m$ domains are essentially identical. Therefore, no further simulations are performed for the $4\lambda_m$ domain.

4.2. *Spanwise domain width* λ_m

4.2.1. *Temporal evolution of the global instability*

To investigate the evolution of the primary global mode, DNS are performed over a sufficiently long physical time in this section. The grid consists of $600 \times 200 \times 40$ cells in the streamwise, wall-normal and spanwise directions, respectively. The flow is initialised by superimposing the most unstable eigenmode $\hat{\boldsymbol{U}}(x, y)$ obtained from 2-D GSA (shown in figure 3*b*) onto a 2-D base flow, as expressed by

$$\boldsymbol{U}_{initial}(x, y, z) = \boldsymbol{U}_{2\text{-}D}(x, y) + \eta\, \mathrm{Re}\left\{\hat{\boldsymbol{U}}(x, y)\, \mathrm{e}^{\mathrm{i}\beta_m z}\right\}. \tag{4.1}$$

In the present case, the perturbation amplitude is set to $\eta = 0.2$ so that the maximum spanwise velocity of the resulting initial flow is approximately one-thousandth of the free-stream velocity, i.e. $\max|w_{initial}| \approx 10^{-3} u_\infty$. The spanwise velocity of the resulting initial flow at the slice $x/L = 1$ is shown in figure 4, corresponding to the global mode with an arbitrary phase. To quantify the evolution of the perturbation, the root mean square (RMS)

https://doi.org/10.1017/jfm.2026.12013 Published online by Cambridge University Press

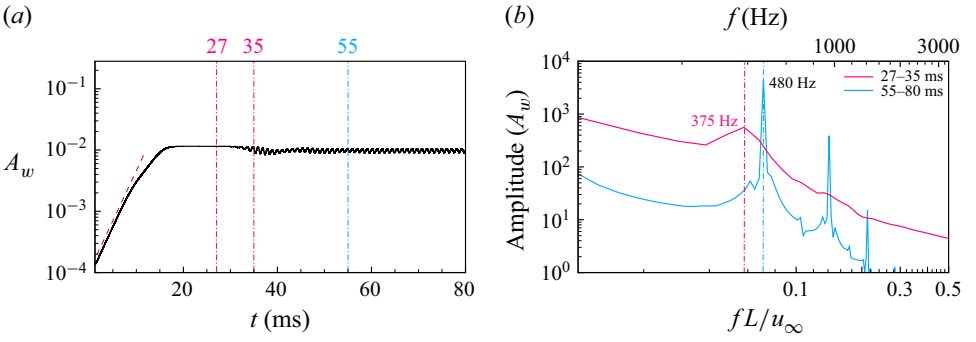


Figure 5. (*a*) Temporal evolution of A_w at the $x/L = 1$ slice in the λ_m domain at $\theta = 32°$, with the dashed line representing the growth rate predicted by 2-D GSA. (*b*) Fourier spectrum of A_w in the unsteady stage.

of spanwise velocity at a given streamwise slice is defined as

$$A_w = \sqrt{\frac{1}{N_y N_z} \sum_{j=1}^{N_y} \sum_{k=1}^{N_z} \left(\frac{w}{u_\infty} \right)^2}, \tag{4.2}$$

where N_y and N_z are the numbers of grid cells in the wall-normal and spanwise directions, respectively. The temporal evolution of A_w at the $x/L = 1$ slice is depicted in figure 5(*a*), with the slope of the red dashed line representing the growth rate predicted by the 2-D GSA. The excellent agreement between the growth rates obtained from DNS and 2-D GSA confirms the growth of the primary global mode. After the linear and subsequent nonlinear growths, the perturbation reaches saturation at approximately $t = 20$ ms. More noteworthy is the emergence of unsteadiness at approximately $t = 31$ ms, manifested as periodic oscillations in the spanwise velocity. During the initial phase of unsteadiness development, the amplitude of perturbation drops slightly and then restores. The reason for this behaviour will be discussed later. Given that only a single stationary global mode is obtained in the 2-D GSA, this unsteady behaviour is conjectured to be associated with a secondary instability, which is a Hopf bifurcation. The grid-independence verification for the 3-D simulation is provided in § A.2.

It should be noted that figure 5(*a*) shows the RMS of spanwise velocity. Since the RMS is based on w^2, a sinusoidal oscillation $w^2(t) \propto \sin^2(\omega t)$ produces an RMS signal that varies with $\sin^2(\omega t) \propto 1 - \cos(2\omega t)$, i.e. with twice the physical frequency. The actual frequency is therefore half of the apparent value inferred from figure 5(*a*). The Fourier spectrum of A_w in the unsteady stage is shown in figure 5(*b*), where the frequency in the horizontal axis has been divided by 2 to reflect the actual frequency. The pink curve represents the initial stage of unsteadiness (27−35 ms), with dominant frequency 375 Hz and Strouhal number $St = fL/u_\infty = 0.056$. The blue curve represents the later stage (55−80 ms), when the unsteadiness has settled into a stable periodic oscillation, with frequency 480 Hz and $St = fL/u_\infty = 0.072$. If the mean separation length L_{sep} is used as the characteristic length, then the corresponding Strouhal numbers $St_{sep} = fL_{sep}/u_\infty$ are 0.053 and 0.068 for these two stages, respectively. This frequency shift is likely associated with the nonlinear effects as the unsteadiness saturates.

The instantaneous spanwise-velocity contours at representative moments are illustrated in figure 6, together with the separation and reattachment lines. In the linear stage (0−8 ms), the perturbation grows exponentially. During the subsequent nonlinear growth

https://doi.org/10.1017/jfm.2026.12013 Published online by Cambridge University Press

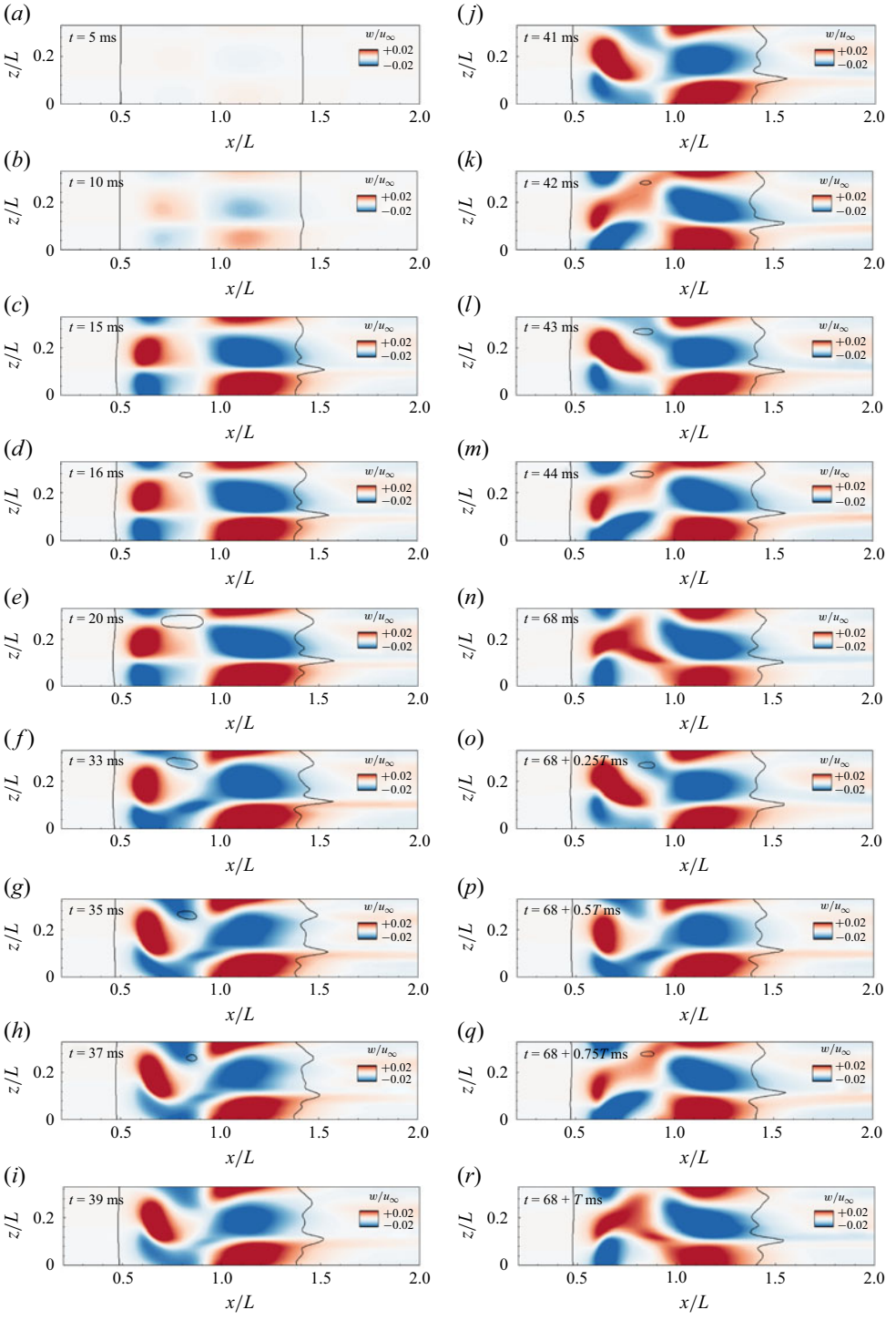


Figure 6. Spanwise velocity contours at representative moments of the $y/L = 0.01$ slice in the λ_m domain at $\theta = 32°$, with the separation and reattachment lines superimposed.

https://doi.org/10.1017/jfm.2026.12013 Published online by Cambridge University Press

(8−18 ms, figures 6*b*,*c*), the reattachment line becomes strongly distorted around the centres of the perturbation waves, and the separation line also exhibits a slight undulating pattern. Meanwhile, a secondary separation emerges between successive pairs of global modes, i.e. in a distance of the wavelength λ_m (this will be seen more clearly in the $2\lambda_m$ domain simulation). The perturbation saturates at approximately 20 ms. Thereafter, the flow field becomes unsteady. In the initial stage of this unsteadiness (see figures 6*f*–*i*), the secondary separation gradually vanishes, accompanied by the decrease of the spanwise velocity amplitude shown in figure 5(*a*). Subsequently, both the secondary separation and the perturbation amplitude recover (figures 6*j*,*k*), and the flow enters a regime of periodic unsteadiness. The evolution over one period of the unsteadiness is shown in figures 6(*n*–*r*). The perturbation exhibits pronounced oscillations in the spanwise direction, accompanied by the intermittent appearance and disappearance of the secondary separation. The unsteadiness seems to be more pronounced in the upstream half of the separation bubble, approximately at $x/L < 1$. The spatial localisation is consistent with the region where the real, viscous shock impingement occurs and the primary global eigenmode reaches its largest amplitude (figure 3*b*). The emergence of both the secondary separation and the unsteadiness can be attributed to the base flow modulation induced by the saturated primary global mode. The complete process of perturbation evolution is illustrated in the supplementary movie 1, available at https://doi.org/10.1017/jfm.2026.12013.

4.2.2. *Bifurcation type and critical angle*

The unsteadiness that emerges after the saturation of the primary stationary global mode indicates the onset of a secondary instability. To identify the bifurcation type (supercritical or subcritical) and determine the corresponding critical angle, a series of DNS cases is carried out with progressively reduced shock angles starting from 32°. The interval between successive angles is 0.2°, and the angle decreases smoothly following a cosine function:

$$\theta = \theta_{initial} - 0.1\left[1 - \cos\left(\pi \frac{k}{k_{total}}\right)\right], \quad k = 1, 2, \ldots, k_{total}. \tag{4.3}$$

Here, $\theta_{initial}$ is the initial angle, k denotes the current time step, and k_{total} is the total number of steps over which the angle is reduced. In the present case, k_{total} is set to 2×10^5, leading to total reduction duration 4 ms. The simulation for each angle is then continued. This smooth cosine variation ensures a continuous transition between shock angles, minimising numerical artefacts during angle reduction. The variation of shock angles is implemented by adjusting the incident position at the inlet boundary and updating the post-shock flow parameters, while the impingement location on the flat plate is kept fixed.

To examine how the unsteadiness disappears as the shock angle is decreased, the spanwise velocity at a representative point ($x/L = 1.125$, $y/L = 0.009$, $z/L = 0.083$) is monitored, as shown in figure 7. At $\theta = 32°$, the spanwise velocity exhibits a clearly periodic oscillation. When the angle is gradually reduced to 31.8°, transient fluctuations arise during the adjustment, but the flow soon re-establishes a stable oscillation with a noticeably smaller amplitude. As the angle decreases further to 31.6°, which is below the critical angle of primary bifurcation ($\theta_c \approx 31.74°$), the oscillation vanishes and the spanwise velocity decays rapidly. This behaviour indicates a transition towards a steady 2-D flow.

Considering that the critical angle for the primary 3-D bifurcation is approximately 31.74°, two additional simulations are performed in which the shock angle is reduced from 31.8° to 31.75° and to 31.7°, respectively. At 31.75°, as indicated by the pink curve, the oscillatory motion decays gradually, demonstrating that the bifurcation associated with

https://doi.org/10.1017/jfm.2026.12013 Published online by Cambridge University Press

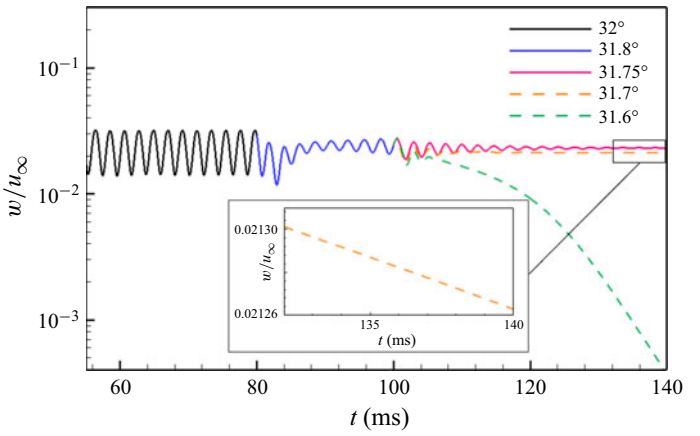


Figure 7. Temporal evolution of the spanwise velocity of a representative point ($x/L = 1.125,\ y/L = 0.009,\ z/L = 0.083$) in the λ_m domain as the shock angle is gradually reduced.

unsteadiness is supercritical and its critical angle lies slightly above 31.75°. At 31.7°, the unsteadiness vanishes completely and the spanwise velocity continues to decay, as shown in the inset of figure 7. This behaviour is consistent with the 2-D GSA prediction that the primary global mode is stable at $\theta = 31.7°$. The weak residual three-dimensionality observed at 31.7° is likely due to the finite simulation time; with a longer simulation time, the three-dimensionality is expected to disappear completely. Both the primary and secondary bifurcations are supercritical and have close critical angles. Importantly, however, their critical angles are distinct: the critical point of the primary pitchfork bifurcation lies below 31.75°, whereas the critical point of the secondary Hopf bifurcation lies above 31.75°. It should be emphasised that a codimension-two bifurcation generically requires two independent control parameters; here, the only control parameter is the shock angle. Therefore, the dynamics corresponds not to a codimension-two point, but simply to a secondary Hopf bifurcation whose critical point is close to the primary bifurcation point.

4.2.3. *The 3-D GSA*

To further investigate the secondary instability of the saturated 3-D flow, 3-D GSA is carried out, which requires a steady base flow. Therefore, for the unsteady flow obtained from the previous DNS, a numerical strategy is required to extract a fixed steady-state solution. The selective frequency damping (SFD) method (Åkervik *et al.* 2006; Jordi *et al.* 2014, 2015) is adopted to obtain a steady state, which has been validated as an efficient approach to filter out unsteadiness at selected frequencies, and to achieve a steady base flow for the 3-D GSA.

The SFD method can be encapsulated in a system as

$$\begin{cases} \dot{\boldsymbol{q}} = \boldsymbol{N}(\boldsymbol{q}) - \chi(\boldsymbol{q} - \bar{\boldsymbol{q}}), \\ \dot{\bar{\boldsymbol{q}}} = \dfrac{\boldsymbol{q} - \bar{\boldsymbol{q}}}{\Delta}. \end{cases} \tag{4.4}$$

Here, $\boldsymbol{q}$ represents the vector of dynamical variables (conservative variables in the present study), and $\boldsymbol{N}$ is the corresponding nonlinear operator. A new target vector $\bar{\boldsymbol{q}}$ of steady-state variables is introduced, with χ serving as the control coefficient in the proportional feedback between $\boldsymbol{q}$ and $\bar{\boldsymbol{q}}$. The parameter Δ defines the width of the low-pass filter. To effectively suppress unsteady oscillations, the parameters χ and Δ must be chosen

https://doi.org/10.1017/jfm.2026.12013 Published online by Cambridge University Press

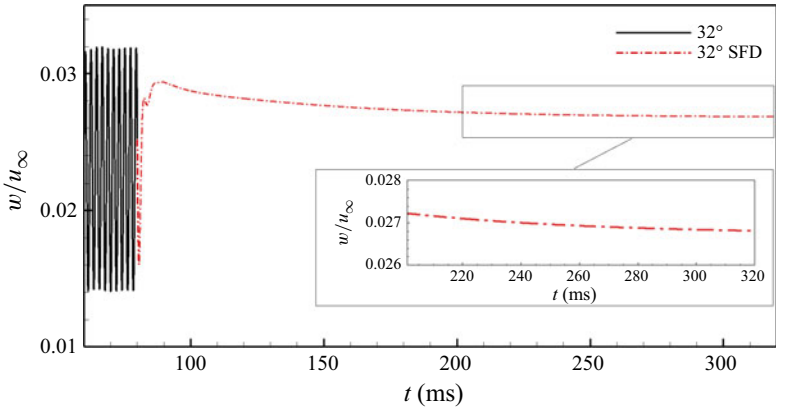


Figure 8. Temporal evolution of the spanwise velocity in the λ_m domain at $\theta = 32°$ of a representative point ($x/L = 1.125,\ y/L = 0.009,\ z/L = 0.083$), with the SFD method turned on at $t = 80$ ms.

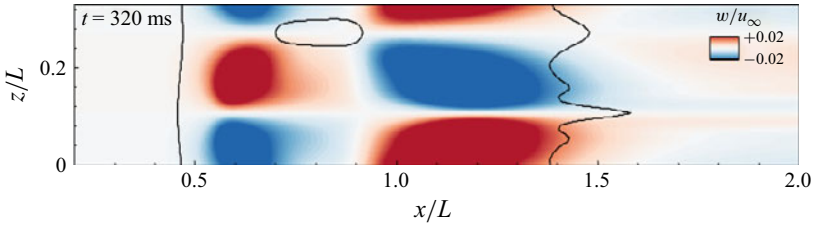


Figure 9. Spanwise velocity contours at $t = 320$ ms of the $y/L = 0.01$ slice in the λ_m domain at $\theta = 32°$, with the separation and reattachment lines superimposed.

appropriately. The cut-off frequency of the filter is given by $f_c = 1/(2\pi\Delta)$, which should be lower than the frequency to be filtered. In § 4.2.1, the dominant frequency of the later unsteady stage observed in DNS is 480 Hz; thus Δ is set to 8×10^{-4}. Following the recommendation of Åkervik *et al.* (2006), the control coefficient can be estimated as $\chi = 1/\Delta = 1250$ when the growth rate of instability is unknown.

Following persistent oscillations at $\theta = 32°$, the SFD method is turned on at $t = 80$ ms. As shown in figure 8, the temporal evolution of spanwise velocity demonstrates that SFD efficiently suppresses the unsteadiness within a short time. However, achieving full convergence to a steady solution remains challenging. Even when the simulation is extended to $t = 320$ ms, the spanwise velocity continues to decay slowly. Nevertheless, the flow field at $t = 320$ ms is considered sufficiently close to steady, and is therefore used as the base flow for the 3-D GSA. As seen in the corresponding spanwise-velocity contour in figure 9, the flow filtered by SFD has restored to a state similar to the saturated flow obtained after the primary growth at $t = 20$ ms (see figure 6*e*). In the temporal evolution shown in figure 5, a relative steady stage exists between the saturation of the primary global mode and the onset of unsteadiness ($20 < t < 30$ ms). To assess the robustness of the 3-D GSA prediction, an additional 3-D GSA is performed using the instantaneous flow at $t = 20$ ms (without SFD influence) as base flow. The corresponding eigenvalue spectrum and eigenmode are presented in § B.1, closely matching those obtained with the SFD-converged base flow. This agreement demonstrates that the 3-D GSA prediction is robust with respect to the choice of base flow, and is not an artefact introduced by SFD.

https://doi.org/10.1017/jfm.2026.12013 Published online by Cambridge University Press

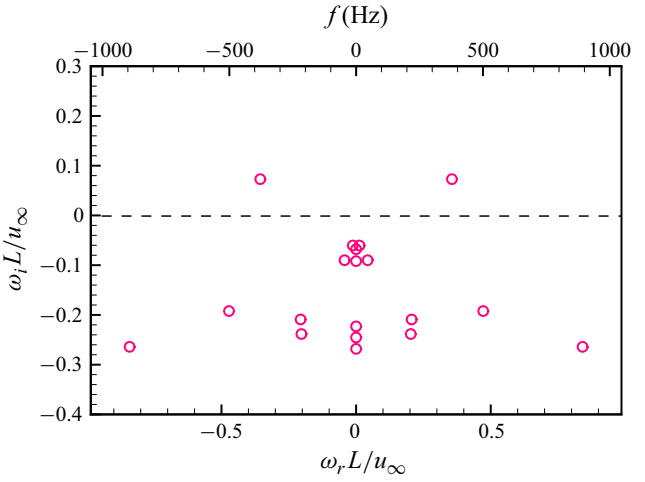


Figure 10. Eigenvalue spectrum obtained from 3-D GSA in the λ_m domain using SFD-converged base flow at $\theta = 32°$.

The 3-D GSA in this study is performed using a second-order Runge–Kutta scheme. The sensitivity to the temporal discretisation is assessed by a validation case with a third-order Runge–Kutta scheme with the same sub-time step as the second-order Runge–Kutta scheme. The resulting eigenvalue spectra are nearly identical, as shown in § B.2. Therefore, the second-order Runge–Kutta scheme is retained for all 3-D GSA calculations for computational efficiency in the current implementation, although higher-order Runge–Kutta schemes are generally preferable when computational cost is acceptable. In addition, the sensitivity to the streamwise domain length is examined by extending the domain length from $2L$ to $2.4L$. As shown in § B.3, the resulting eigenvalue spectrum is unchanged, confirming that the present streamwise domain is sufficiently long to obtain accurate 3-D GSA results. The grid used in 3-D GSA consists of 600×200 cells in the streamwise and wall-normal directions, for which grid-independence has been verified for 2-D GSA and DNS (§§ A.1 and A.2). In the spanwise direction, the grid resolution is then refined from 40 to 80 cells by linear interpolation of the SFD-converged solution. Grid independence in the spanwise direction is examined specifically for the 3-D GSA, and is reported in § A.3.

The eigenvalue spectrum using the base flow with 80 spanwise cells is shown in figure 10. A pair of unstable oscillatory modes is identified, confirming the Hopf bifurcation inferred from the DNS. The physical frequency of this unsteady mode is 378 Hz, which closely matches the frequency in the initial stage of unsteadiness (375 Hz) measured in the DNS. The higher frequency (480 Hz) of the later stage in DNS is thought to be related to the distorted base flow caused by the nonlinear effect, which differs from the SFD-converged base flow. This distortion may be associated with the mean-flow correction described as 'shift-mode' in Noack *et al.* (2003), although a dedicated modal analysis would be required to establish this connection.

The corresponding eigenmode is illustrated in figure 11. The mode is primarily concentrated within the separation bubble, and extends downstream as streamwise-elongated structures that alternate in sign in the spanwise direction. These oppositely signed structures are likely to be the origin of the high- and low-speed streaks. These streaks are unsteady, as shown in the supplementary movie 1, because they are associated

https://doi.org/10.1017/jfm.2026.12013 Published online by Cambridge University Press

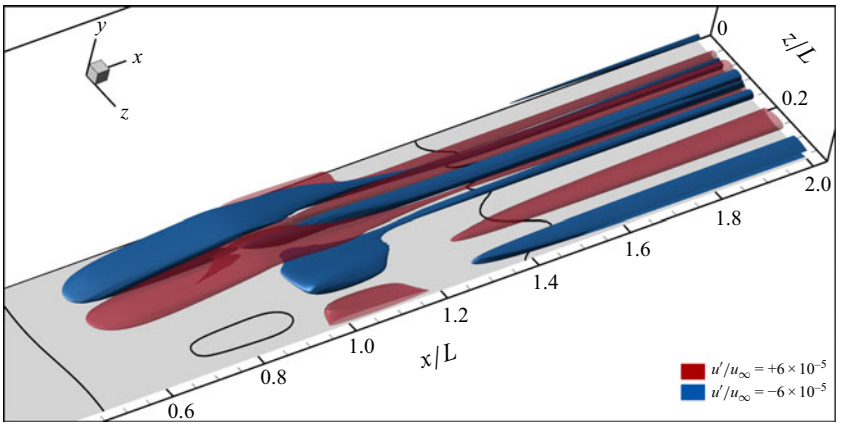


Figure 11. Eigenmode obtained from 3-D GSA in the λ_m domain using SFD-converged base flow at $\theta = 32°$, with iso-surfaces of the streamwise velocity. Black lines represent the separation and reattachment lines.

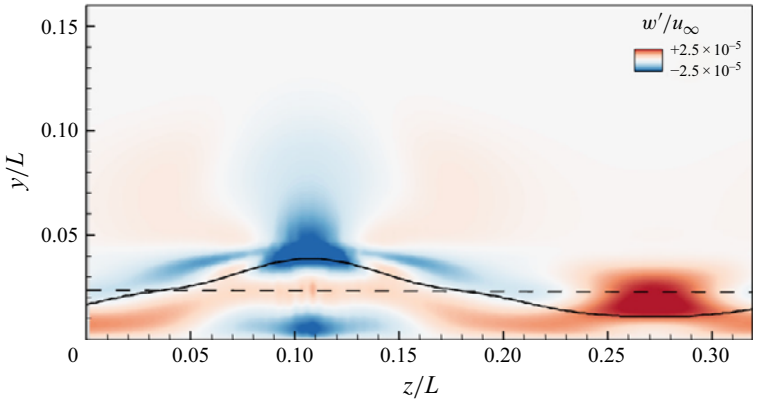


Figure 12. Spanwise velocity perturbation contour of the $x/L = 1$ slice of the eigenmode obtained from 3-D GSA in the λ_m domain at $\theta = 32°$. The solid black line indicates the edge of the reversed region in the SFD-converged 3-D flow; the dashed black line indicates the edge of the reversed region in the nominal 2-D flow.

with the oscillatory global mode. The dominant eigenmode amplitude is absent inside the secondary separation bubble, indicating that the secondary separation may not be crucial to the unsteadiness. A slice at $x/L = 1$ is extracted, and the spanwise-velocity contour is shown in figure 12. When the contour is superimposed with the edges of reversed regions from the 3-D and 2-D flows, it is evident that the maximum perturbation occurs in the region where the base flow is most severely distorted. This distortion is induced by the evolution of the primary global mode. A similar localisation of perturbation was reported by Rodríguez *et al.* (2021) for the secondary instability of incompressible laminar separation bubbles: the most unstable eigenmode (distorted planar Kelvin–Helmholtz waves) concentrates near the maximum reversed flow. This observation suggests that the base flow modulation provides the most likely origin for the secondary global instability, which will be further investigated in a future study.

https://doi.org/10.1017/jfm.2026.12013 Published online by Cambridge University Press

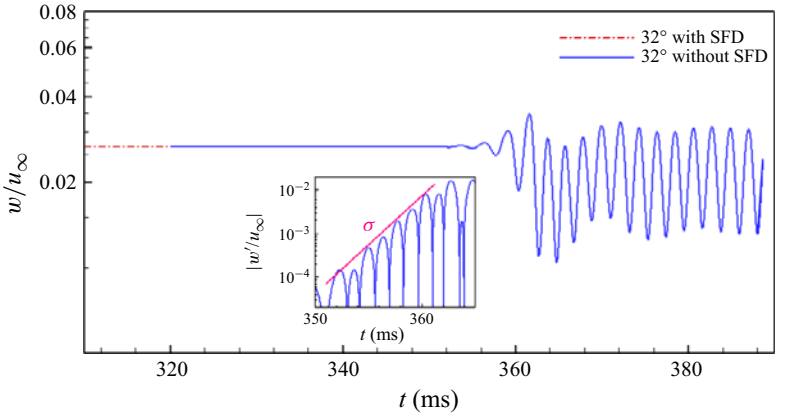


Figure 13. Temporal evolution of the spanwise velocity in the λ_m domain at $\theta = 32°$ of a representative point ($x/L = 1.125$, $y/L = 0.009$, $z/L = 0.083$), with the SFD method turned off at $t = 320$ ms. The pink line indicates the growth rate predicted by 3-D GSA.

4.2.4. *Validation of the secondary instability: unsteadiness*

To validate the 3-D GSA results, the SFD method is turned off to allow the perturbation to grow naturally again. The simulation is initialised from a flow field at $t = 320$ ms, which is sufficiently damped by SFD. As shown in figure 13, the unsteadiness begins to develop at approximately $t = 350$ ms. Similar to the behaviour observed in figure 5(*a*), the perturbation amplitude decreases at approximately $t = 362$ ms, then recovers and settles into a periodic oscillation. The frequency of this newly developed unsteadiness is initially 370 Hz, then shifts to 480 Hz. These frequencies are consistent with those observed in the first development of unsteadiness before the activation of the SFD method (figure 5*b*). The lower frequency is also close to the value predicted by 3-D GSA (378 Hz). This agreement suggests that the early stage of unsteadiness is predominantly governed by linear dynamics. As the unsteadiness reaches the nonlinear stage, the effective base flow is modified by the nonlinear interaction, so that it differs from the SFD-converged base flow. This distortion of base flow provides an explanation for the frequency shift towards the higher saturated value 480 Hz.

To isolate the growth of unsteadiness, the perturbation is obtained by subtracting the SFD-converged base flow:

$$\boldsymbol{U}' = \boldsymbol{U} - \boldsymbol{U}_{SFD}, \tag{4.5}$$

where $\boldsymbol{U}_{SFD}$ denotes the vector of flow variables fully damped by SFD at $t = 320$ ms. In particular, the spanwise perturbation is plotted in the inset of figure 13. The growth rate from this extracted perturbation signal agrees very well with that predicted by the 3-D GSA, as indicated by the pink line. Correspondingly, the perturbation field at $t = 358$ ms extracted using (4.5) is shown in figure 14. This perturbation field closely resembles the 3-D GSA eigenmode shown in figure 11.

Therefore, based on the above analysis, in the computational domain with spanwise width λ_m, the unsteadiness observed in the DNS is a secondary instability that develops from the saturated flow after the growth of the primary global mode. This secondary instability gives rise to a Hopf bifurcation in the flow, which is classified as supercritical with a critical angle slightly above 31.75°.

https://doi.org/10.1017/jfm.2026.12013 Published online by Cambridge University Press

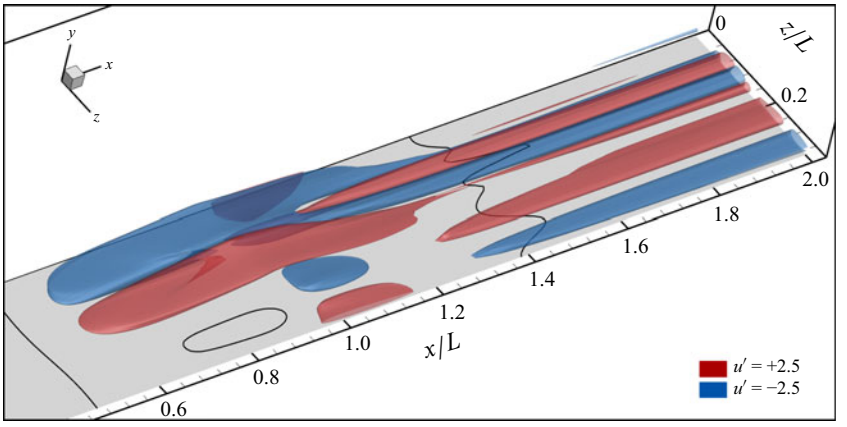


Figure 14. Perturbation field extracted at $t = 358$ ms with SFD turned off in the λ_m domain at $\theta = 32°$, with iso-surfaces of the streamwise velocity perturbation.

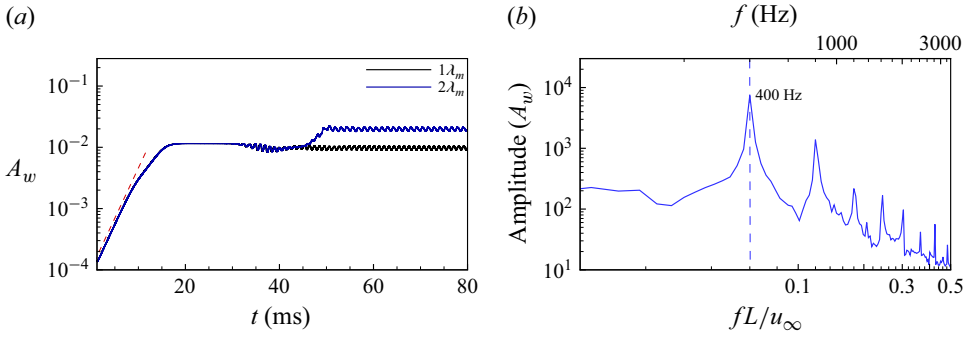


Figure 15. (*a*) Temporal evolution of A_w at the $x/L = 1$ slice in the $2\lambda_m$ domain at $\theta = 32°$, with the dashed line representing the growth rate predicted by 2-D GSA. (*b*) Fourier spectrum of A_w in the unsteady stage (60−80 ms).

4.3. *Spanwise domain width* $2\lambda_m$

4.3.1. *Temporal evolution of the global instability*

As in the λ_m case, the investigation of the $2\lambda_m$ domain also begins with the temporal evolution of the primary global mode. The DNS in the $2\lambda_m$ domain are performed using a grid of $600 \times 200 \times 80$ cells in the streamwise, wall-normal and spanwise directions, respectively. The initial flow is also constructed by superimposing the primary global mode on the 2-D base flow, as illustrated in (4.1) with $\eta = 0.2$. The evolution of the spanwise velocity indicator A_w, defined by (4.2), is shown in figure 15(*a*). The linear growth, nonlinear growth, perturbation saturation of the primary global mode and initial development of secondary unsteady instability in the $2\lambda_m$ domain are essentially identical to those observed in the λ_m domain. The clear deviation appears at $t \approx 42$ ms, when a secondary growth of the perturbation occurs. Following this secondary growth, the flow exhibits a periodic oscillation similar to that in the λ_m domain. Once again, it should be noted that because A_w is based on w^2, the apparent frequency in figure 15(*a*) is twice the actual physical frequency. The corresponding Fourier spectrum with the frequency axis

https://doi.org/10.1017/jfm.2026.12013 Published online by Cambridge University Press

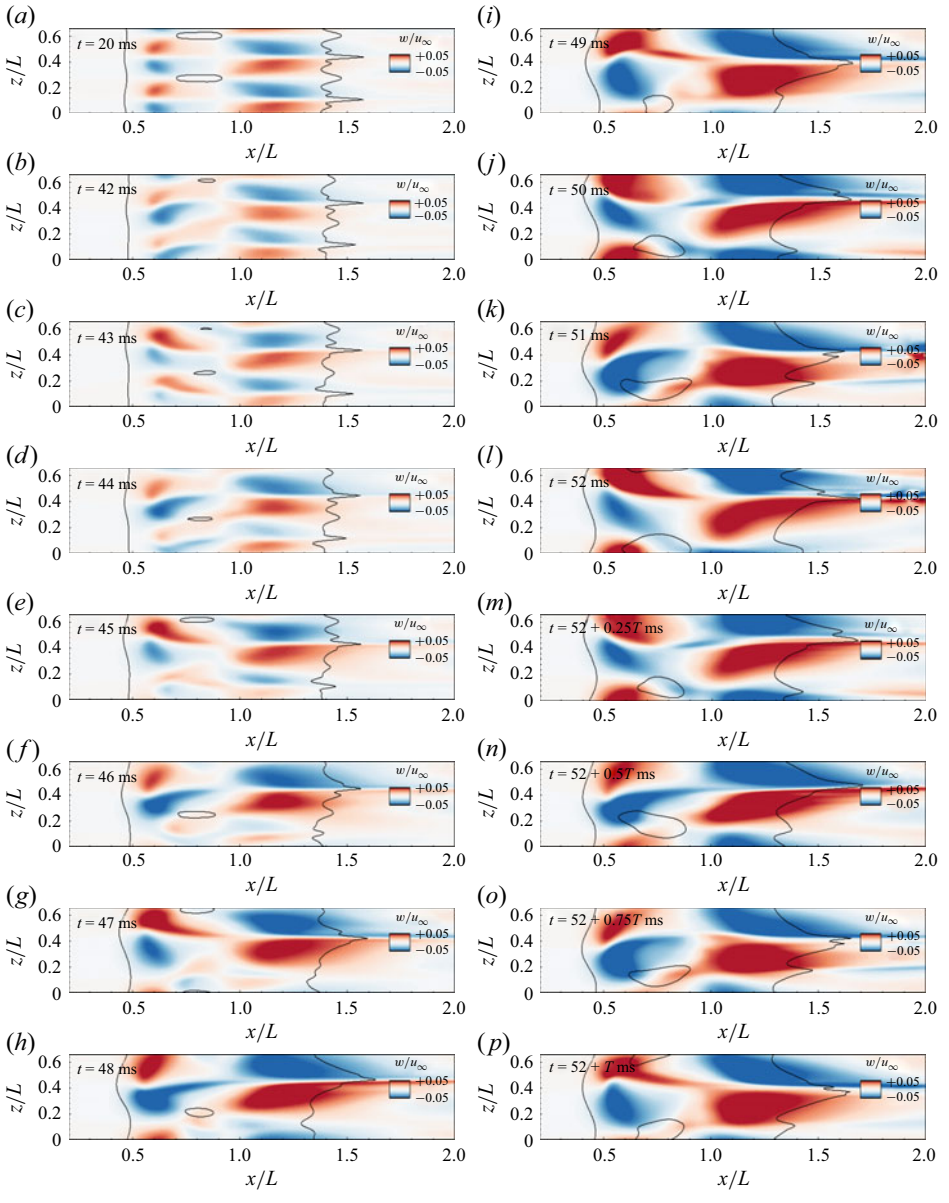


Figure 16. Spanwise velocity contours at representative moments of the $y/L = 0.01$ slice in the $2\lambda_m$ domain at $\theta = 32°$, with the separation and reattachment lines superimposed.

divided by 2 to recover the actual frequency is shown in figure 15(*b*). The unsteadiness frequency in the $2\lambda_m$ domain is $f \approx 400$ Hz, which differs from $f \approx 480$ Hz observed in the later stage of the unsteadiness in the λ_m domain. This difference arises from the change in flow dynamics, which will be discussed later.

The evolution of flow structures during perturbation growth is illustrated by instantaneous contours of spanwise velocity in figure 16. When interpreted with figure 15, the flow evolution in the $2\lambda_m$ domain becomes clear. After the linear and nonlinear growth of the primary global mode, the λ_m-wavelength primary perturbation has saturated

https://doi.org/10.1017/jfm.2026.12013 Published online by Cambridge University Press

at $t = 20$ ms (figure 16*a*). At this stage, two spanwise wavelengths of the global mode present within the $2\lambda_m$ domain and two secondary separation bubbles are trapped between neighbouring pairs of perturbation waves. Then the secondary unsteady instability of λ_m spanwise wavelength develops at $t \approx 27$ ms, followed by a secondary-growth phase starting at $t \approx 42$ ms. As the secondary growth sets in, one pair of the perturbation waves weakens while the other pair strengthens, and the number of secondary separation bubbles reduces from 2 to 1 (figures 16*b–h*). The strengthened pair progressively dominates the computational domain; by $t = 49$ ms, the spanwise wavelength has increased to $2\lambda_m$. Subsequently, the remaining secondary separation bubble enlarges, and the distortions of both the separation and reattachment lines are markedly more pronounced (figures 16*i–l*). In the end, the flow settles into a periodic oscillation (figures 16*l–p*) with frequency 400 Hz. The difference between saturated frequencies in the λ_m domain (480 Hz) and the $2\lambda_m$ domain (400 Hz) is explained by the wavelength doubling in the $2\lambda_m$ domain, which allows a larger wavelength and hence a lower frequency.

The perturbation evolution in the $2\lambda_m$ domain observed in DNS can be summarised into four stages: (i) linear and nonlinear growth of the primary global mode with λ_m wavelength; (ii) unsteadiness with λ_m wavelength after saturation of the primary global mode; (iii) a secondary growth accompanied by wavelength doubling into $2\lambda_m$; and (iv) a periodic unsteadiness with $2\lambda_m$ wavelength. The evolution process is provided in the supplementary movie 2.

4.3.2. *Bifurcation type and critical angle*

Compared with the case of the λ_m domain, the dynamics in the $2\lambda_m$ domain is more complex. In addition to the unsteadiness, the secondary growth emerges, accompanied by the wavelength doubling. As demonstrated in § 4.2.2, the unsteadiness in the λ_m domain arises through a supercritical bifurcation. Here, the same angle-reduction strategy is employed to determine the bifurcation types associated with the secondary growth in the $2\lambda_m$ domain.

The temporal evolution of the spanwise velocity is plotted in figure 17 to visualise the perturbation variation. As the shock angle is reduced, the oscillation amplitude decreases progressively. At $\theta = 31.2°$, the unsteadiness vanishes, and the remaining three-dimensionality continues to approach zero as shown in the inset of figure 17. Note that the spanwise velocity at the measured point is negative. If the simulation time is sufficiently long, then the three-dimensionality is expected to vanish at $\theta = 31.2°$. Given that the critical angle of the primary global mode is $\theta_c \approx 31.74°$, the persistence of three-dimensionality and stable periodic unsteadiness below θ_c indicates that the bifurcation associated with the secondary growth and the accompanied wavelength doubling is subcritical. This is further supported by the spanwise-velocity contour of the $x/L = 1$ slice at $\theta = 31.2°$ (figure 18), which shows that the perturbation retains wavelength $2\lambda_m$. The threshold for the subcritical secondary growth lies between 31.4° and 31.2°. Regarding the unsteadiness observed below 31.74°, the presence of the subcritical secondary-growth branch alters the post-saturation dynamics, allowing unsteadiness in the $2\lambda_m$ domain to persist over a wider range of shock angles, down to $\theta = 31.4°$.

4.3.3. *Validation of the secondary instability: secondary growth*

The secondary growth is most likely to be attributed to a secondary instability of the saturated primary global mode, and thus shares the same underlying physical origin as the unsteadiness. A more speculative alternative is that it represents an instability that develops only after the onset of unsteadiness. To clarify the origin of this secondary growth,

https://doi.org/10.1017/jfm.2026.12013 Published online by Cambridge University Press

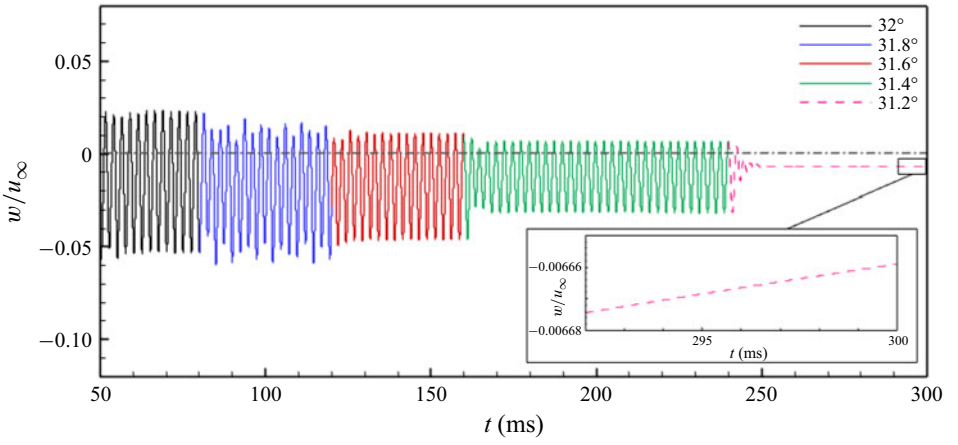


Figure 17. Temporal evolution of the spanwise velocity of a representative point $(x/L = 1.125,\ y/L = 0.009,\ z/L = 0.083)$ in the $2\lambda_m$ domain as the shock angle is gradually reduced.

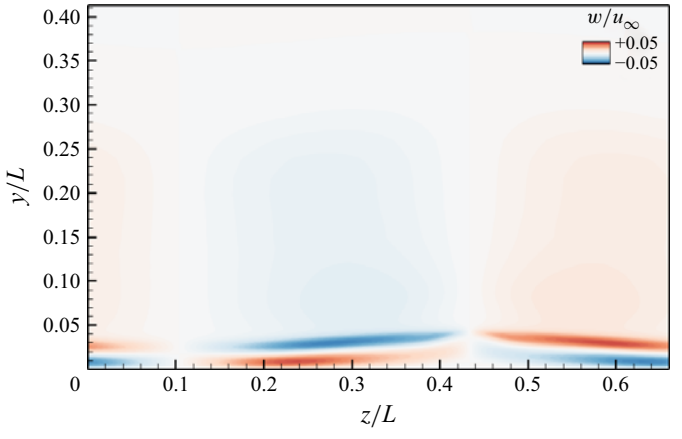


Figure 18. Spanwise velocity contour of the $x/L = 1$ slice at $\theta = 31.2°$ in the $2\lambda_m$ domain.

an additional simulation is restarted from $t = 25$ ms with the SFD method activated. The initial condition is taken as the instantaneous flow field obtained at $t = 25$ ms, i.e. after the saturation of the primary global mode in the $2\lambda_m$ domain as shown in figure 15. The corresponding evolution of A_w is shown in figure 19. When the unsteadiness is suppressed by SFD, a secondary growth of the perturbation still develops following saturation of the primary mode. Its onset is, however, markedly delayed, because with SFD there is only the $2\lambda_m$ steady mode. By contrast, without SFD (blue curve), two unstable modes are present: one λ_m unsteady mode and one $2\lambda_m$ steady mode. The behaviour in the $2\lambda_m$ domain with SFD supports the interpretation of the secondary growth as a genuine secondary instability of the primary global mode, rather than an instability developing on the unsteady branch.

Therefore, for the case with spanwise domain width $2\lambda_m$, both the unsteadiness and the secondary growth are attributed to secondary instabilities of the saturated primary global mode. The latter is associated with spanwise wavelength $2\lambda_m$, manifesting itself as the observed wavelength doubling. In terms of bifurcation types, the secondary growth

https://doi.org/10.1017/jfm.2026.12013 Published online by Cambridge University Press

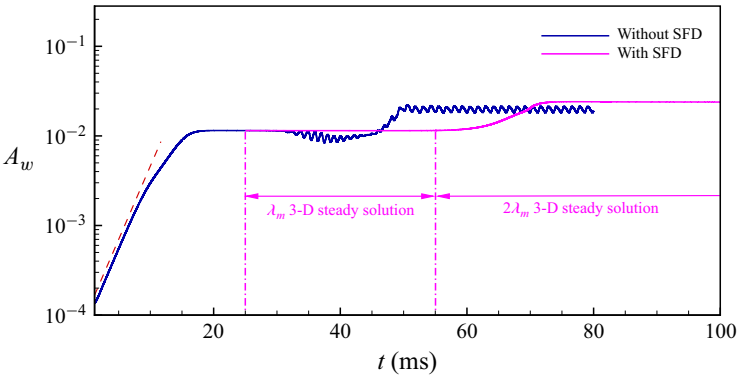


Figure 19. Temporal evolution of A_w at the $x/L = 1$ slice at $\theta = 32°$ in the $2\lambda_m$ domain, with and without the SFD method.

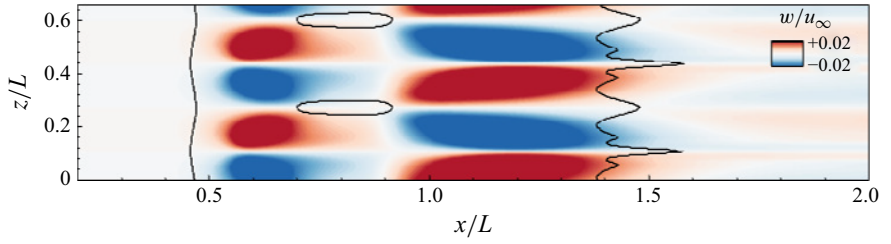


Figure 20. Spanwise velocity contour of duplicated SFD-converged solution in the $2\lambda_m$ domain at $\theta = 32°$.

undergoes a subcritical bifurcation with a critical angle between 31.4° and 31.2°. The subcritical nature of this secondary growth is evidenced by the persistence of the 3-D component below the primary critical angle $\theta_c \approx 31.74°$, implying hysteresis in the appearance and disappearance of the 3-D perturbation. It is also worth noting that in the natural DNS evolution without SFD, the naked steady secondary branch is invisible, as the unsteady dynamics inherited from the λ_m wavelength effectively masks the underlying steady behaviour.

4.3.4. *The 3-D GSA*

Previous numerical simulations with and without SFD rule out the possibility that the secondary growth originates from the limit cycle. Otherwise, a Floquet analysis must be considered. Instead, 3-D GSA is performed in the $2\lambda_m$ domain to characterise the secondary-instability behaviour. The base flow is constructed by duplicating the SFD-converged λ_m-domain solution (flow field at $t = 320$ ms in figure 9) to span a $2\lambda_m$ domain. As a result, two copies of the λ_m primary structure exist in the newly constructed $2\lambda_m$-width base flow, as shown in figure 20. The number of grid cells in the spanwise direction is 160, yielding the same spanwise grid resolution as in the λ_m-domain 3-D GSA case.

The resulting eigenvalue spectrum is shown in figure 21. Two unstable modes are identified: one unsteady mode with a larger growth rate, and one steady mode with a lower growth rate. The corresponding eigenmodes are presented in figure 22. For the unsteady mode, the spanwise wavelength is λ_m, and the frequency is 378 Hz. Both the frequency and the spatial structure closely resemble those of the mode obtained in the λ_m

https://doi.org/10.1017/jfm.2026.12013 Published online by Cambridge University Press

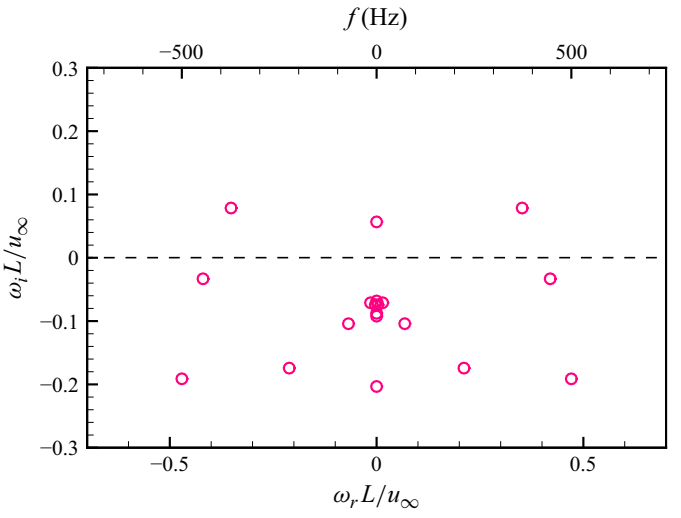


Figure 21. Eigenvalue spectrum obtained from 3-D GSA in the $2\lambda_m$ domain at $\theta = 32°$ using SFD-converged base flow.

domain (figures 10 and 11). In contrast, the steady mode exhibits wavelength $2\lambda_m$, thereby providing a direct explanation for the wavelength-doubling behaviour observed in DNS. Moreover, the higher growth rate of the unsteady mode is consistent with the earlier onset of unsteadiness relative to the secondary growth observed in DNS. Under the combined influence of these two unstable modes, the flow ultimately evolves towards an unsteady state characterised by a dominant $2\lambda_m$ wavelength.

As shown in figure 15, the temporal evolution of the perturbation also presents a short steady stage over $20 < t < 30$ ms. Thus an additional 3-D GSA is performed using the snapshot base flow at $t = 20$ ms, as reported in § B.1. Consistent with the λ_m case, both the eigenvalue spectrum and eigenmode structures are essentially unchanged relative to those obtained with the SFD-converged base flow, indicating that the 3-D GSA prediction is robust.

5. Discussions and conclusions

This paper presents a combined DNS and 3-D GSA investigation of the secondary global instabilities arising from the saturated primary mode in the interaction between an oblique shock and a laminar boundary layer at Mach 2.15. The DNS are used to establish the flow evolution and the onset scenarios in different spanwise domains, whereas 3-D GSA provides the modal interpretation and identifies the relevant secondary instability branches.

We first revisit the primary global instability using 2-D GSA, and determine the corresponding critical shock angle to $\theta_c \approx 31.74°$. At $\theta = 32°$, the flow contains a single stationary unstable global mode with spanwise wavelength λ_m. The DNS are then performed at 32° in spanwise domains of widths λ_m and $2\lambda_m$.

In the λ_m domain, saturation of the primary global mode is followed by the onset of unsteadiness, with dominant frequencies 375 Hz ($St_{sep} = 0.053$) in the early stage, and 480 Hz ($St_{sep} = 0.068$) in the later stage. As the shock angle is gradually reduced, this unsteadiness disappears at $\theta = 31.75°$, indicating that the critical angle for unsteadiness

https://doi.org/10.1017/jfm.2026.12013 Published online by Cambridge University Press

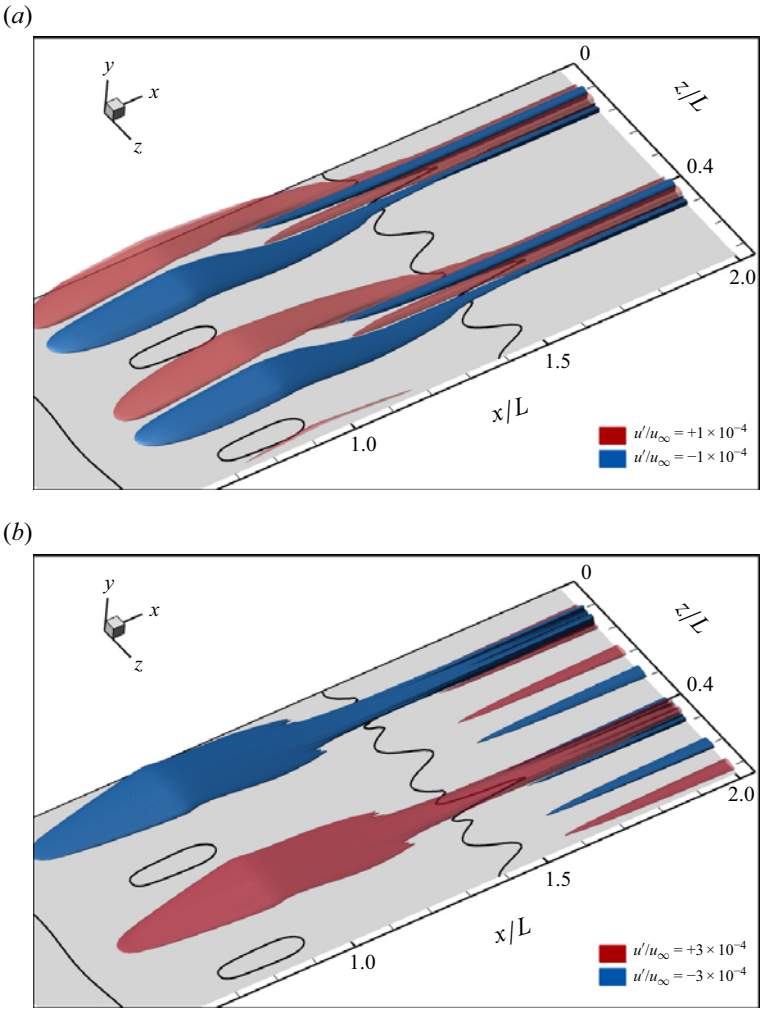


Figure 22. Eigenmodes obtained from 3-D GSA in the $2\lambda_m$ domain at $\theta = 32°$ using the SFD-converged base flow of (*a*) the unsteady mode and (*b*) the steady mode, with iso-surfaces of the streamwise velocity.

lies slightly above 31.75°. The smooth attenuation of the oscillation amplitude as shock angle decreases suggests that the unsteadiness is associated with a supercritical Hopf bifurcation. To obtain a steady base flow for 3-D GSA, the SFD method is applied to suppress the oscillatory dynamics. The 3-D GSA based on the resulting SFD-converged base flow identifies an unsteady secondary mode with frequency 378 Hz. This frequency closely matches that observed during the early stage of unsteadiness in DNS (375 Hz), which is dominated by the linear dynamics. The higher frequency 480 Hz observed in the later stage of DNS is influenced by the nonlinear effects. The existence of this unsteady secondary instability is further confirmed by switching off SFD in DNS: the unsteadiness re-emerges, and the growth rate, frequency and spatial structure of the perturbation closely match the 3-D GSA prediction.

The investigation is then extended to the $2\lambda_m$ domain. The DNS show that after saturation of the primary global mode, unsteadiness first develops, followed by a secondary growth accompanied by wavelength doubling. The frequency of unsteadiness after the

https://doi.org/10.1017/jfm.2026.12013 Published online by Cambridge University Press

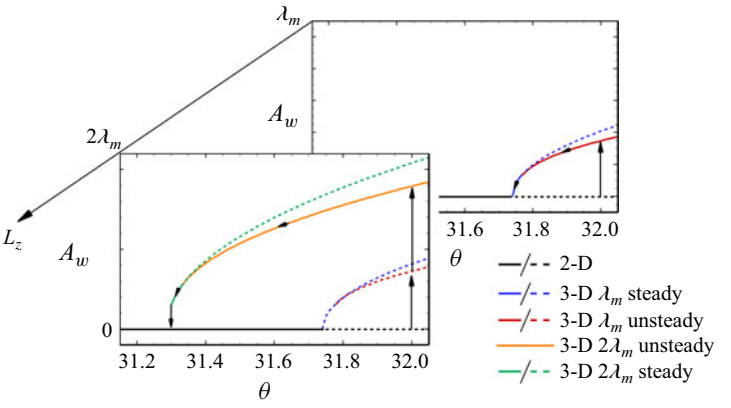


Figure 23. Schematic of the bifurcations as functions of shock angle θ, perturbation amplitude A_w and spanwise width L_z. (The value of amplitude A_w and its variation with shock angle θ are shown for illustration only.)

secondary growth is approximately 400 Hz. Using the angle-reduction procedure as in the λ_m domain, the unsteadiness disappears at 31.2°, and the three-dimensionality keeps decaying. Given that the critical angle of the primary global mode is $\theta_c \approx 31.74°$, this hysteresis implies a subcritical bifurcation of secondary growth, with a critical angle between 31.4° and 31.2°. To clarify the origin of secondary growth, additional DNS are performed in the $2\lambda_m$ domain with the SFD method activated. The results show that even in the absence of unsteadiness, the secondary growth still develops. This demonstrates that secondary growth constitutes an independent secondary instability of the saturated primary global mode, rather than an instability relying on the unsteady branch. The 3-D GSA is then performed in the $2\lambda_m$ domain using a base flow constructed by duplicating the SFD-converged solution from the λ_m domain. Two unstable modes are identified. The first is an unsteady mode with spanwise wavelength λ_m, whose frequency and eigenmode closely resemble those obtained in the λ_m domain. The second is a steady mode with wavelength $2\lambda_m$, providing the modal origin of the secondary growth and the wavelength doubling observed in DNS. The unsteady mode has a larger growth rate than the steady mode, consistent with the earlier onset of unsteadiness relative to the secondary growth presented in DNS.

Based on the above discussion, the overall scenario can be summarised as shown in figure 23, where the arrows show DNS procedures. When the flow is globally unstable, a stationary primary global mode occurs with critical angle $\theta_c \approx 31.74°$ (blue branch). Saturation of this mode gives rise to secondary instabilities. In the λ_m domain, the secondary Hopf bifurcation appears with its critical angle slightly above 31.75° (red branch). The spanwise-velocity amplitude A_w of the steady branch is larger than that of the unsteady branch, as implied in the DNS results. When the spanwise domain is enlarged to $2\lambda_m$, an additional steady mode with wavelength $2\lambda_m$ appears, driving the flow to the $2\lambda_m$ unsteady branch (orange). This branch is subcritical, with critical angle between 31.4° and 31.2°, as indicated by the reducing-angle DNS. Consequently, for shock angles between the critical angle of the $2\lambda_m$ unsteady branch and the primary critical angle ($\theta_c \approx 31.74°$), two solutions coexist: a 2-D steady flow and a 3-D unsteady flow, whose realisation depends on the initial perturbation. The subcritical 3-D unsteady state can only be triggered by finite-amplitude perturbations, and persists below the primary critical angle. The $2\lambda_m$ steady branch (green) is masked by the unsteady dynamics and is observed only at smaller angles.

https://doi.org/10.1017/jfm.2026.12013 Published online by Cambridge University Press

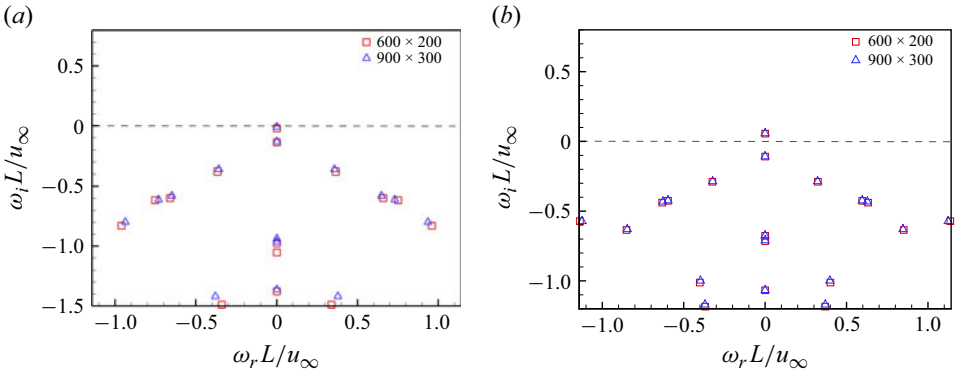


Figure 24. Eigenvalue spectra obtained from 2-D GSA for different grid resolutions at (*a*) $\theta = 31.7°$ and (*b*) $\theta = 32°$.

Additional 3-D GSA is conducted at $\theta = 31.4°$ and $\theta = 31.2°$ to validate the $2\lambda_m$ unsteady branch, which is provided in Appendix C.

To the authors' knowledge, this is the first study to systematically characterise secondary global instabilities in supersonic SWBLIs. A sequence of bifurcations leading to unsteady dynamics at the characteristic frequency of the low-frequency unsteadiness in SWBLIs is thus identified. The distinct behaviours obtained in the λ_m and $2\lambda_m$ domains further highlight that the flow dynamics (especially the low-frequency dynamics) depend sensitively on the chosen spanwise domain widths. In the wider domain, the subcritical nature of the secondary bifurcation suggests the possibility of a bifurcation from the 2-D steady branch to the 3-D unsteady branch triggered by finite amplitude forcing. Although this triggering remains to be investigated, it points to a potentially important role of upstream forcing in establishing the low-frequency dynamics of SWBLIs. The mechanism of secondary global instability in this paper is linked to the base flow modulation induced by the primary global instability, while a more precise identification of the origin is left for future adjoint-based wavemaker analysis.

Supplementary movies. Supplementary movies are available at https://doi.org/10.1017/jfm.2026.12013.

Funding. This work is supported by the National Natural Science Foundation of China (no. 12472239) and the Hong Kong Research Grants Council (no. 15234025).

Declaration of interests. The authors report no conflict of interest.

Appendix A. Grid-independence verification

A.1 *The 2-D GSA*

The grid-independence verification for 2-D GSA is performed using grids of 600×200 and 900×300 cells in the streamwise and wall-normal directions. As shown in figure 24, the corresponding eigenvalue spectra at 31.7° and 32° obtained on the two grids are nearly identical, indicating that the 600×200 grid provides grid-independent results.

A.2 *The 3-D DNS*

For the 3-D DNS, the grid-independence verification is carried out using grids of $600 \times 200 \times 40$ and $900 \times 300 \times 80$ cells at shock angle 32°. The temporal evolution of A_w at the $x/L = 1$ slice for both grids is presented in figure 25. The linear and nonlinear growth

https://doi.org/10.1017/jfm.2026.12013 Published online by Cambridge University Press

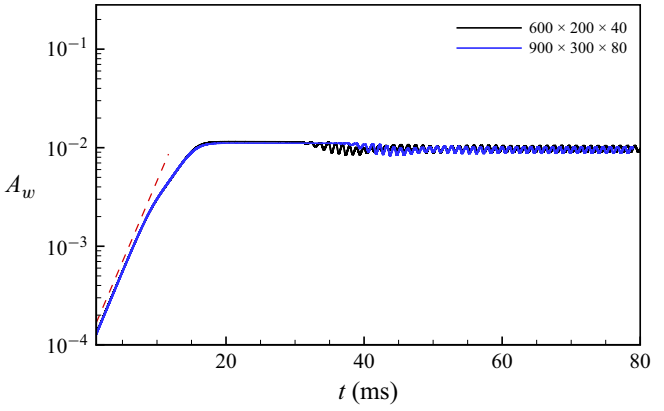


Figure 25. Comparison of the temporal evolution of A_w at the $x/L = 1$ slice in the λ_m domain at $\theta = 32°$, for different grid resolutions.

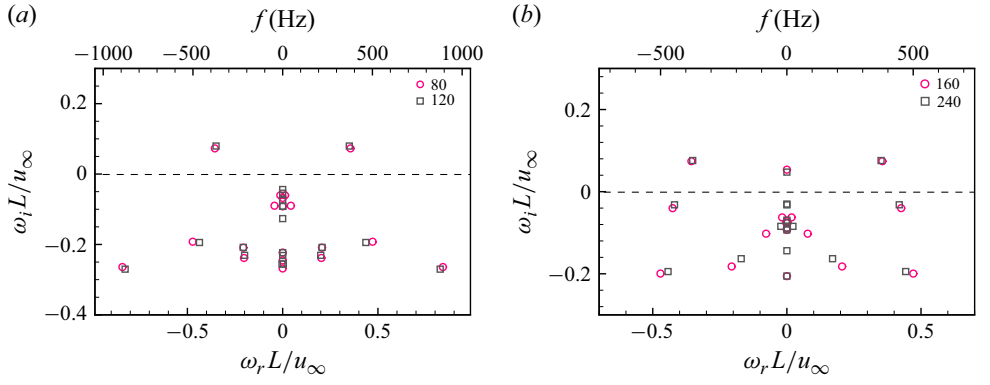


Figure 26. Eigenvalue spectra obtained from 3-D GSA of different spanwise grid resolutions at $\theta = 32°$ in the (*a*) λ_m and (*b*) $2\lambda_m$ domains.

stages, as well as the amplitudes of the saturated perturbation, are almost the same for both grids. The only noticeable difference is that the finer grid exhibits a slightly delayed onset of unsteadiness. This delay is likely due to the lower level of numerical errors (e.g. round-off errors) in the finer grid, which affects the triggering of the secondary instability. Nevertheless, the frequency and the amplitude of oscillation in the unsteady stage are almost identical for the two grids. Therefore, a $600 \times 200 \times 40$ grid is sufficient to achieve grid independence for the perturbation evolution in the 3-D simulation.

A.3 *The 3-D GSA*

For 3-D GSA, the grid of 600×200 cells in the streamwise and wall-normal directions is sufficiently fine, as confirmed by the grid-independence verification for 2-D GSA. In the spanwise direction, the resolution is refined to 80 and 120 cells over width λ_m by linear interpolation of DNS results. The corresponding eigenvalue spectra for λ_m and $2\lambda_m$ domains are plotted in figure 26. The spanwise resolution with 80 cells over λ_m width is already sufficient to capture the eigenmodes, in particular the unstable modes.

https://doi.org/10.1017/jfm.2026.12013 Published online by Cambridge University Press

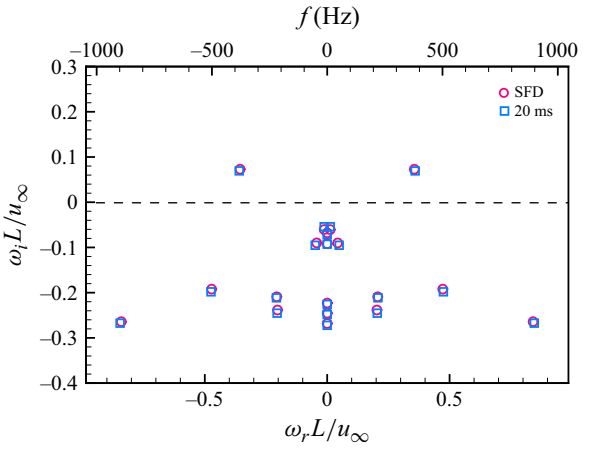


Figure 27. Eigenvalue spectra in the λ_m domain obtained from 3-D GSA using the $t = 20$ ms base flow and the SFD-converged base flow at $\theta = 32°$.

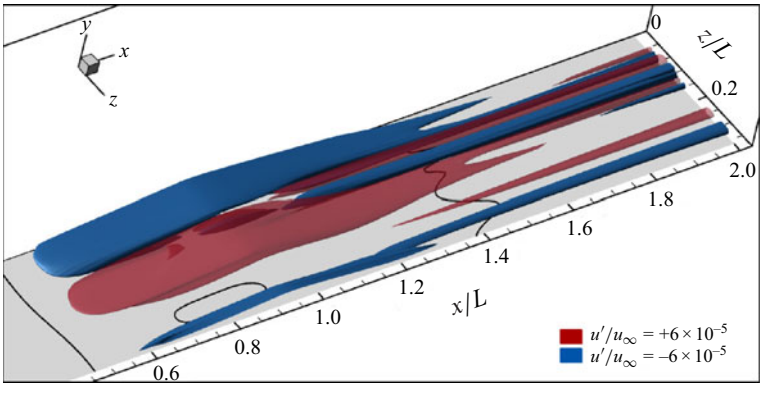


Figure 28. Eigenmode in the λ_m domain obtained from 3-D GSA using the $t = 20$ ms base flow at $\theta = 32°$.

Appendix B. Validation cases for 3-D GSA

B.1 *The 3-D GSA using the base flows at 20 ms*

In the λ_m domain, the eigenvalue spectrum and the corresponding eigenmode obtained using the $t = 20$ ms base flow are shown in figures 27 and 28, respectively. Compared with the results based on the SFD-converged base flow (figure 11), the eigenvalues are in very close agreement, and the eigenmodes exhibit essentially the same spatial structure. In the $2\lambda_m$ domain, the 3-D GSA results based on the $t = 20$ ms snapshot are shown in figures 29 and 30. In terms of eigenvalues, both the unsteady and steady modes agree well with those obtained from the SFD-converged base flow. For eigenmodes, the steady mode remains highly consistent between the two base flows, whereas the spatial structure of the unsteady mode exhibits a slight difference (figures 22*a* and 30*a*), likely due to residual time dependence in the snapshot base flow. Overall, the 3-D GSA predictions are robust to the base-flow definition since both base flows yield nearly identical eigenvalue spectra and similar eigenmodes.

https://doi.org/10.1017/jfm.2026.12013 Published online by Cambridge University Press

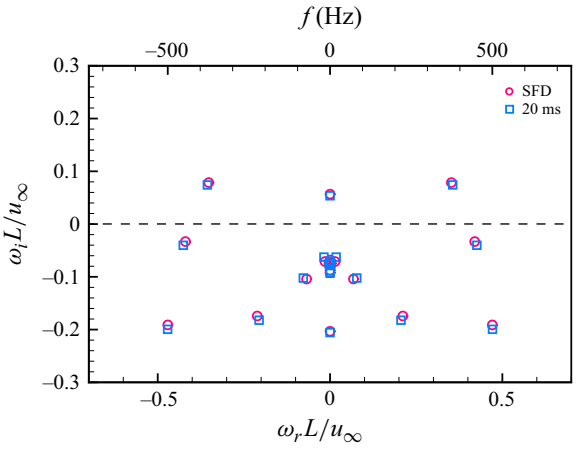


Figure 29. Eigenvalue spectra in the $2\lambda_m$ domain obtained from 3-D GSA using the $t = 20$ ms base flow and the SFD-converged base flow at $\theta = 32°$.

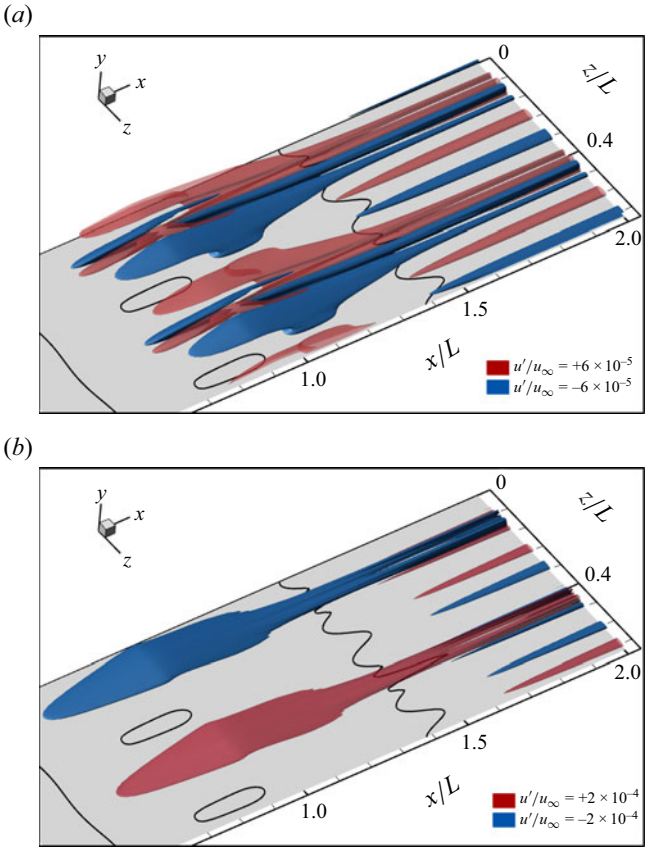


Figure 30. Eigenmodes in the $2\lambda_m$ domain obtained from 3-D GSA using the $t = 20$ ms base flow at $\theta = 32°$: (*a*) unsteady mode and (*b*) steady mode, with iso-surfaces of the streamwise velocity.

https://doi.org/10.1017/jfm.2026.12013 Published online by Cambridge University Press

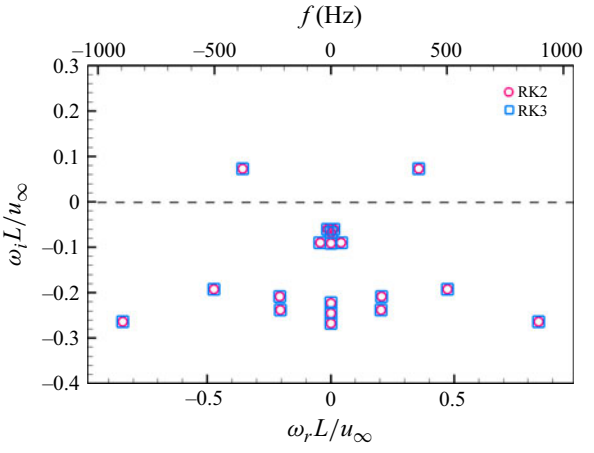


Figure 31. Eigenvalue spectra in the λ_m domain obtained from 3-D GSA using the second-order (RK2) and third-order (RK3) Runge–Kutta schemes at $\theta = 32°$.

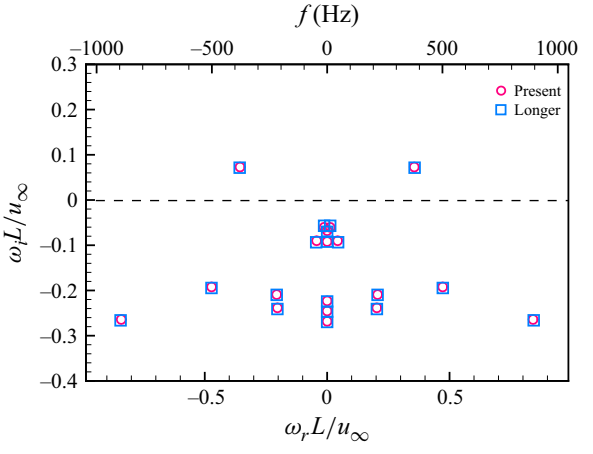


Figure 32. Eigenvalue spectra in the λ_m domain obtained from 3-D GSA using the longer streamwise domain and the present domain at $\theta = 32°$.

B.2 *The 3-D GSA using a third-order Runge–Kutta time scheme*

To assess the sensitivity of 3-D GSA results to temporal discretisation, a comparison between the second-order and third-order Runge–Kutta schemes is presented in figure 31. In this comparison, the same sub-time step is used for both schemes to isolate the influence of the time scheme. The corresponding eigenvalue spectra are almost identical, confirming that the identified secondary instability is insensitive to the choice of time scheme. Therefore, the second-order Runge–Kutta scheme is employed in the remaining 3-D GSA calculations for computational efficiency in the current case. Nevertheless, higher-order Runge–Kutta schemes with more favourable stability properties are generally preferable when the additional computational cost is acceptable.

https://doi.org/10.1017/jfm.2026.12013 Published online by Cambridge University Press

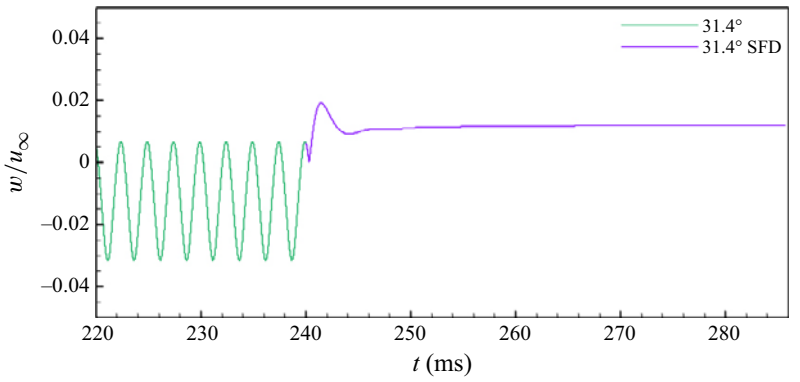


Figure 33. Temporal evolution of the spanwise velocity at $\theta = 31.4°$ in the $2\lambda_m$ domain of a representative point ($x/L = 1.125,\ y/L = 0.009,\ z/L = 0.083$), with the SFD method turned on at $t = 240$ ms.

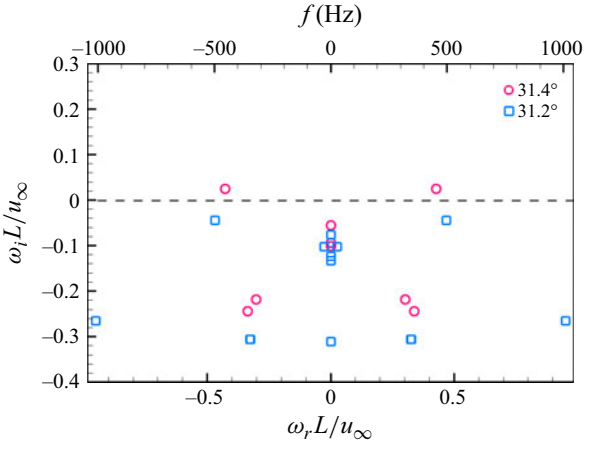


Figure 34. Eigenvalue spectra in the $2\lambda_m$ domain obtained from 3-D GSA at $\theta = 31.4°$ and $\theta = 31.2°$.

B.3 *The 3-D GSA in a longer streamwise domain*

The sensitivity of 3-D GSA to the streamwise domain length is examined using an extended computational domain. The downstream boundary is moved from $x = 2L$ to $x = 2.4L$, increasing the number of streamwise grid cells to 664. The original grid is retained, and additional cells are introduced only in the extended region between $x = 2L$ and $x = 2.4L$. The base flow is recomputed in the longer domain, and the flow field at $t = 20$ ms is utilised as the base flow for 3-D GSA. The resulting eigenvalue spectrum is shown in figure 32. The spectrum is nearly identical to that obtained in the original domain, demonstrating that extending the streamwise domain has a negligible influence on the 3-D GSA results.

Appendix C. The 3-D GSA at $\theta = 31.4°$ and $\theta = 31.2°$

To validate the $2\lambda_m$ unsteady branch, 3-D GSA is performed at $\theta = 31.4°$ in the $2\lambda_m$ domain. The base flow is obtained by activating SFD at $t = 240$ ms (figure 17).

https://doi.org/10.1017/jfm.2026.12013 Published online by Cambridge University Press

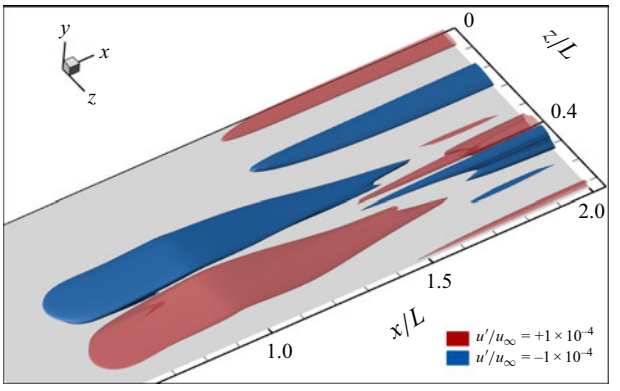


Figure 35. Eigenmode in the $2\lambda_m$ domain obtained from 3-D GSA at $\theta = 31.4°$.

The temporal evolution of the spanwise velocity is plotted in figure 33. It is seen that the SFD method effectively suppresses oscillations, and the resulting steady solution at $t = 286$ ms is then used as the base flow for 3-D GSA. Note that this base flow comprises one $2\lambda_m$ structure. As shown by the eigenvalue spectrum in figure 34, one unstable mode is identified at $\theta = 31.4°$, corresponding to an unsteady mode with frequency 450 Hz. The associated eigenmode structure (figure 35) is similar to the λ_m unsteady eigenmode (figures 11 and 22*a*) while exhibiting spanwise wavelength $2\lambda_m$, thereby confirming the existence of the $2\lambda_m$ unsteady branch shown in figure 23. A further 3-D GSA is conducted at $\theta = 31.2°$ using the base flow at $t = 300$ ms as shown in figure 17. The eigenvalue spectrum (blue symbols in figure 34) demonstrates that no unstable mode is present at $\theta = 31.2°$. Therefore, the critical angle for this $2\lambda_m$ unsteady branch lies between 31.4° and 31.2°, consistent with the DNS results.

References

Ackeret, J., Feldmann, F. & Rott, N. 1947 Investigations of compression shocks and boundary layers in gases moving at high speed. *NACA Tech. Rep.* No. 1113. National Advisory Committee for Aeronautics (NACA).

Åkervik, E., Brandt, L., Henningson, D.S., Hœpffner, J., Marxen, O. & Schlatter, P. 2006 Steady solutions of the Navier–Stokes equations by selective frequency damping. *Phys. Fluids* **18** (6), 068102.

Amestoy, P.R., Buttari, A., L'Excellent, J.Y. & Mary, T. 2019 Performance and scalability of the block low-rank multifrontal factorization on multicore architectures. *ACM Trans. Math. Softw.* **45** (1), 1–26.

Amestoy, P.R., Duff, I.S., L'Excellent, J.Y. & Koster, J. 2001 A fully asynchronous multifrontal solver using distributed dynamic scheduling. *SIAM J. Matrix Anal. Appl.* **23** (1), 15–41.

Bagheri, S., Schlatter, P., Schmid, P.J. & Henningson, D. 2009 Global stability of a jet in crossflow. *J. Fluid Mech.* **624**, 33–44.

Balakumar, P. & Malik, M.R. 1992 Discrete modes and continuous spectra in supersonic boundary layers. *J. Fluid Mech.* **239**, 631–656.

Balakumar, P., Zhao, H. & Atkins, H. 2005 Stability of hypersonic boundary layers over a compression corner. *AIAA J.* **43** (4), 760–767.

Barkley, D., Blackburn, H.M. & Sherwin, S.J. 2008 Direct optimal growth analysis for timesteppers. *Intl J. Numer. Meth. Fluids* **57** (9), 1435–1458.

Ben Hassan Saïdi, I., Wang, S., Fournier, G., Tenaud, C. & Robinet, J.C. 2025 Modal analysis of the triadic interactions in the dynamics of a transitional shock wave boundary layer interaction. *J. Fluid Mech.* **1009**, A43.

Brusniak, L. & Dolling, D.S. 1994 Physics of unsteady blunt-fin-induced shock wave/turbulent boundary layer interactions. *J. Fluid Mech.* **273**, 375–409.

https://doi.org/10.1017/jfm.2026.12013 Published online by Cambridge University Press

CHANG, C.L. & MALIK, M.R. 1994 Oblique-mode breakdown and secondary instability in supersonic boundary layers. *J. Fluid Mech.* **273**, 323–360.
CHAPMAN, D.R., KUEHN, D.M. & LARSON, H.K. 1958 Investigation of separated flows in supersonic and subsonic streams with emphasis on the effect of transition. *NACA Tech. Rep.* NACA-TR-1356. National Advisory Committee for Aeronautics (NACA).
CLEMENS, N.T. & NARAYANASWAMY, V. 2014 Low-frequency unsteadiness of shock wave/turbulent boundary layer interactions. *Annu. Rev. Fluid Mech.* **46** (1), 469–492.
DEGREZ, G., BOCCADORO, C.H. & WENDT, J.F. 1987 The interaction of an oblique shock wave with a laminar boundary layer revisited. An experimental and numerical study. *J. Fluid Mech.* **177**, 247–263.
DÉLERY, J., MARVIN, J.G. & RESHOTKO, E. 1986 Shock-wave boundary layer interactions. NASA STI/Recon *Tech. Rep.* AGARD-AG-280. North Atlantic Treaty Organization, Advisory Group for Aerospace Research and Development (AGARD).
DOLLING, D.S. 2001 Fifty years of shock-wave/boundary-layer interaction research: what next? *AIAA J.* **39** (8), 1517–1531.
DONALDSON, C.D. 1944 *Effects of Interaction between Normal Shock and Boundary Layer*. NACA.
DUPONT, P., HADDAD, C. & DEBIEVE, J.F. 2006 Space and time organization in a shock-induced separated boundary layer. *J. Fluid Mech.* **559**, 255–277.
DUSSAUGE, J.-P., DUPONT, P. & DEBIÈVE, J.F. 2006 Unsteadiness in shock wave boundary layer interactions with separation. *Aerosp. Sci. Technol.* **10** (2), 85–91.
DUSSAUGE, J.-P. & PIPONNIAU, S. 2008 Shock/boundary-layer interactions: possible sources of unsteadiness. *J. Fluids Struct.* **24** (8), 1166–1175.
DWIVEDI, A., SIDHARTH, G.S. & JOVANOVIĆ, M.R. 2022 Oblique transition in hypersonic double-wedge flow. *J. Fluid Mech.* **948**, A37.
DWIVEDI, A., SIDHARTH, G.S., NICHOLS, J.W., CANDLER, G.V. & JOVANOVIĆ, M.R. 2019 Reattachment streaks in hypersonic compression ramp flow: an input–output analysis. *J. Fluid Mech.* **880**, 113–135.
ERDOS, J. & PALLONE, A. 1962 Shock–boundary layer interaction and flow separation. In *Proceedings of the Heat Transfer and Fluid Mechanics Institute* (ed. F.E. Ehlers, J.J. Kauzlarich, C.A. Sleicher Jr. & R.E. Street), vol. 15, pp. 239–254. Stanford University Press.
ERENGIL, M.E. & DOLLING, D.S. 1991 Unsteady wave structure near separation in a Mach 5 compression ramp interaction. *AIAA J.* **29** (5), 728–735.
FASEL, H., THUMM, A. & BESTEK, H. 1993 Direct numerical simulation of transition in supersonic boundary layers: oblique breakdown. In *Transitional and Turbulent Compressible Flows* (ed. L.D. Kral & T.A. Zang), vol. FED 151, pp. 77–92. ASME.
FEDOROV, A.V. & KHOKHLOV, A.P. 1991 Excitation of unstable modes in a supersonic boundary layer by acoustic waves. *Fluid Dyn.* **26** (4), 531–537.
FRANTZ, R.A.S., MIMEAU, C., SALIHOGLU, M., LOISEAU, J.C. & ROBINET, J.C. 2025 Bifurcation sequence in the wakes of a sphere and a cube. *J. Fluid Mech.* **1018**, A30.
GADD, G.E. 1957 A theoretical investigation of laminar separation in supersonic flow. *J. Aeronaut. Sci.* **24** (10), 759–771.
GANAPATHISUBRAMANI, B., CLEMENS, N.T. & DOLLING, D.S. 2007 Effects of upstream boundary layer on the unsteadiness of shock-induced separation. *J. Fluid Mech.* **585**, 369–394.
GIANNETTI, F., LUCHINI, P. & MARINO, L. 2009 Linear stability analysis of three-dimensional lid-driven cavity flow. In *Atti del 19th Congresso AIMETA di Meccanica Teorica e Applicata*, vol. 738. Aras Edizioni.
HANKEY, W.L. JR & HOLDEN, M.S. 1975 Two-dimensional shock wave-boundary layer interactions in high speed flows. *Tech. Rep.* AGARD-AG-203. North Atlantic Treaty Organization, Advisory Group for Aerospace Research and Development (AGARD).
HAO, J. 2023 On the low-frequency unsteadiness in shock wave–turbulent boundary layer interactions. *J. Fluid Mech.* **971**, A28.
HAO, J., CAO, S., GUO, P. & WEN, C.Y. 2023 Response of hypersonic compression corner flow to upstream disturbances. *J. Fluid Mech.* **964**, A25.
HAO, J., CAO, S., WEN, C.Y. & OLIVIER, H. 2021 Occurrence of global instability in hypersonic compression corner flow. *J. Fluid Mech.* **919**, A4.
HAO, J., WANG, J. & LEE, C.H. 2016 Numerical study of hypersonic flows over reentry configurations with different chemical nonequilibrium models. *Acta Astronaut.* **126**, 1–10.
HAO, J. & WEN, C.Y. 2020 Hypersonic flow over spherically blunted double cones. *J. Fluid Mech.* **896**, A26.
HARTEN, A., LAX, P.D. & VAN LEER, B. 1983 On upstream differencing and Godunov-type schemes for hyperbolic conservation laws. *SIAM Rev.* **25** (1), 35–61.
HE, W. & TIMME, S. 2021 Triglobal infinite-wing shock-buffet study. *J. Fluid Mech.* **925**, A27.

https://doi.org/10.1017/jfm.2026.12013 Published online by Cambridge University Press

HENDRICKSON, T.R., KARTHA, A. & CANDLER, G.V. 2018 An improved Ducros sensor for the simulation of compressible flows with shocks. In *2018 Fluid Dynamics Conference*, p. 3710. American Institute of Aeronautics and Astronautics (AIAA).

HILDEBRAND, N., DWIVEDI, A., NICHOLS, J.W., JOVANOVIĆ, M.R. & CANDLER, G.V. 2018 Simulation and stability analysis of oblique shock-wave/boundary-layer interactions at Mach 5.92. *Phys. Rev. Fluids* **3** (1), 013906.

JORDI, B.E., COTTER, C.J. & SHERWIN, S.J. 2014 Encapsulated formulation of the selective frequency damping method. *Phys. Fluids* **26** (3), 034101.

JORDI, B.E., COTTER, C.J. & SHERWIN, S.J. 2015 An adaptive selective frequency damping method. *Phys. Fluids* **27** (9), 094104.

KACHANOV, Y.S. 1994 Physical mechanisms of laminar-boundary-layer transition. *Annu. Rev. Fluid Mech.* **26**, 411–482.

VAN LEER, B. 1979 Towards the ultimate conservative difference scheme. V. A second-order sequel to Godunov's method. *J. Comput. Phys.* **32** (1), 101–136.

LI, C. & HAO, J. 2023 Global stability of supersonic flow over a hollow cylinder/flare. *J. Fluid Mech.* **975**, A40.

LIEPMANN, H.W. 1946 The interaction between boundary layer and shock waves in transonic flow. *J. Aeronaut. Sci.* **13** (12), 623–637.

LIGHTHILL, M.J. 1953 On boundary layers and upstream influence II. Supersonic flows without separation. *Proc. R. Soc. Lond. A: Math. Phys. Sci.* **217** (1131), 478–507.

LOISEAU, J.C., ROBINET, J.C., CHERUBINI, S. & LERICHE, E. 2014 Investigation of the roughness-induced transition: global stability analyses and direct numerical simulations. *J. Fluid Mech.* **760**, 175–211.

LUGRIN, M., BENEDDINE, S., LECLERCQ, C., GARNIER, E. & BUR, R. 2021 Transition scenario in hypersonic axisymmetrical compression ramp flow. *J. Fluid Mech.* **907**, A6.

MACCORMACK, R.W. 2014 *Numerical Computation of Compressible and Viscous Flow*. American Institute of Aeronautics and Astronautics, Inc.

MACK, L.M. 1984 Boundary-layer linear stability theory. *Tech. Rep.* AGARD Report No. 709, Part 3. California Inst of Tech Pasadena Jet Propulsion Lab.

MALIK, M.R. 1989 Prediction and control of transition in supersonic and hypersonic boundary layers. *AIAA J.* **27** (11), 1487–1493.

MAURIELLO, M., SHARMA, P.K., LARCHEVÊQUE, L. & SANDHAM, N. 2025 Role of nonlinearities induced by deterministic forcing in the low-frequency dynamics of transitional shock wave/boundary layer interaction. *J. Fluid Mech.* **1016**, A6.

NICHOLS, J.W., LARSSON, J., BERNARDINI, M. & PIROZZOLI, S. 2017 Stability and modal analysis of shock/boundary layer interactions. *Theor. Comput. Fluid Dyn.* **31** (1), 33–50.

NOACK, B.R., AFANASIEV, K., MORZYŃSKI, M., TADMOR, G. & THIELE, F. 2003 A hierarchy of low-dimensional models for the transient and post-transient cylinder wake. *J. Fluid Mech.* **497**, 335–363.

PAGELLA, A., BABUCKE, A. & RIST, U. 2004 Two-dimensional numerical investigations of small-amplitude disturbances in a boundary layer at $Ma = 4.8$: compression corner versus impinging shock wave. *Phys. Fluids* **16** (7), 2272–2281.

REYHNER, T.A. & FLÜGGE-LOTZ, I. 1968 The interaction of a shock wave with a laminar boundary layer. *Intl J. Non-Linear Mech.* **3** (2), 173–199.

ROBINET, J.C. 2007 Bifurcations in shock-wave/laminar-boundary-layer interaction: global instability approach. *J. Fluid Mech.* **579**, 85–112.

RODRÍGUEZ, D., GENNARO, E.M. & SOUZA, L.F. 2021 Self-excited primary and secondary instability of laminar separation bubbles. *J. Fluid Mech.* **906**, A13.

SABNIS, K. & BABINSKY, H. 2023 A review of three-dimensional shock wave–boundary-layer interactions. *Prog. Aerosp. Sci.* **143**, 100953.

SANDHAM, N.D. & REYNOLDS, W. 1991 Three-dimensional simulations of large eddies in the compressible mixing layer. *J. Fluid Mech.* **224**, 133–158.

SANDHAM, N.D., SCHÜLEIN, E., WAGNER, A., WILLEMS, S. & STEELANT, J. 2014 Transitional shock-wave/boundary-layer interactions in hypersonic flow. *J. Fluid Mech.* **752**, 349–382.

SANSICA, A., OHMICHI, Y., ROBINET, J.C. & HASHIMOTO, A. 2020 Laminar supersonic sphere wake unstable bifurcations. *Phys. Fluids* **32** (12), 126107.

SANSICA, A., ROBINET, J.C., ALIZARD, F. & GONCALVES, E. 2018 Three-dimensional instability of a flow past a sphere: Mach evolution of the regular and Hopf bifurcations. *J. Fluid Mech.* **855**, 1088–1115.

SAVARINO, F., POULAIN, A., SIPP, D. & RIGAS, G. 2024 Optimal transitional mechanisms in oblique shock wave–boundary layer interaction using non-linear input/output analysis. In *AIAA SCITECH 2024 Forum*, *AIAA Paper* 2024-2552. American Institute of Aeronautics and Astronautics (AIAA).

https://doi.org/10.1017/jfm.2026.12013 Published online by Cambridge University Press

SIDHARTH, G., DWIVEDI, A., CANDLER, G.V. & NICHOLS, J.W. 2018 Onset of three-dimensionality in supersonic flow over a slender double wedge. *Phys. Rev. Fluids* **3** (9), 093901.

SONG, Z. & HAO, J. 2023 Global instability of the interaction between an oblique shock and a laminar boundary layer. *Phys. Fluids* **35** (8), 084121.

SONG, Z. & HAO, J. 2025 Instabilities in shock-wave–boundary-layer interactions at Mach 6. *J. Fluid Mech.* **1019**, A28.

SORENSEN, D., LEHOUCQ, R., YANG, C. & MASCHHOFF, K. 1996 ARPACK software, version 2.3. Available at: http://www.caam.rice.edu/software/ARPACK.

STANEWSKY, E. 1988 Shock boundary layer interaction. In *AGARD, Boundary Layer Simulation and Control in Wind Tunnels* (ed. M.L. Laster), pp. 271–305. North Atlantic Treaty Organization, Advisory Group for Aerospace Research and Development (AGARD).

STEWARTSON, K. & WILLIAMS, P.G. 1969 Self-induced separation. *Proc. R. Soc. Lond. A: Math. Phys. Sci.* **312** (1509), 181–206.

TEZUKA, A. & SUZUKI, K. 2006 Three-dimensional global linear stability analysis of flow around a spheroid. *AIAA J.* **44** (8), 1697–1708.

THEOFILIS, V. 2011 Global linear instability. *Annu. Rev. Fluid Mech.* **43** (1), 319–352.

TORO, E.F., SPRUCE, M. & SPEARES, W. 1994 Restoration of the contact surface in the HLL-Riemann solver. *Shock Waves* **4**, 25–34.

ZHONG, X. & WANG, X. 2012 Direct numerical simulation on the receptivity, instability, and transition of hypersonic boundary layers. *Annu. Rev. Fluid Mech.* **44** (1), 527–561.

https://doi.org/10.1017/jfm.2026.12013 Published online by Cambridge University Press